

NASA/TM-2014-218291



Hydrogen-Bonding Surfaces for Ice Mitigation

*Joseph G. Smith Jr. and Christopher J. Wohl
Langley Research Center, Hampton, Virginia*

*Richard E. Kreeger
Glenn Research Center, Cleveland, Ohio*

*Kevin R. Hadley and Nicholas McDougall
South Dakota School of Mines & Technology, Rapid City, South Dakota*

July 2014

NASA STI Program . . . in Profile

Since its founding, NASA has been dedicated to the advancement of aeronautics and space science. The NASA scientific and technical information (STI) program plays a key part in helping NASA maintain this important role.

The NASA STI program operates under the auspices of the Agency Chief Information Officer. It collects, organizes, provides for archiving, and disseminates NASA's STI. The NASA STI program provides access to the NASA Aeronautics and Space Database and its public interface, the NASA Technical Report Server, thus providing one of the largest collections of aeronautical and space science STI in the world. Results are published in both non-NASA channels and by NASA in the NASA STI Report Series, which includes the following report types:

- **TECHNICAL PUBLICATION.** Reports of completed research or a major significant phase of research that present the results of NASA Programs and include extensive data or theoretical analysis. Includes compilations of significant scientific and technical data and information deemed to be of continuing reference value. NASA counterpart of peer-reviewed formal professional papers, but having less stringent limitations on manuscript length and extent of graphic presentations.
- **TECHNICAL MEMORANDUM.** Scientific and technical findings that are preliminary or of specialized interest, e.g., quick release reports, working papers, and bibliographies that contain minimal annotation. Does not contain extensive analysis.
- **CONTRACTOR REPORT.** Scientific and technical findings by NASA-sponsored contractors and grantees.

- **CONFERENCE PUBLICATION.** Collected papers from scientific and technical conferences, symposia, seminars, or other meetings sponsored or co-sponsored by NASA.
- **SPECIAL PUBLICATION.** Scientific, technical, or historical information from NASA programs, projects, and missions, often concerned with subjects having substantial public interest.
- **TECHNICAL TRANSLATION.** English-language translations of foreign scientific and technical material pertinent to NASA's mission.

Specialized services also include organizing and publishing research results, distributing specialized research announcements and feeds, providing information desk and personal search support, and enabling data exchange services.

For more information about the NASA STI program, see the following:

- Access the NASA STI program home page at <http://www.sti.nasa.gov>
- E-mail your question to help@sti.nasa.gov
- Fax your question to the NASA STI Information Desk at 443-757-5803
- Phone the NASA STI Information Desk at 443-757-5802
- Write to:
STI Information Desk
NASA Center for AeroSpace Information
7115 Standard Drive
Hanover, MD 21076-1320

NASA/TM-2014-218291



Hydrogen-Bonding Surfaces for Ice Mitigation

*Joseph G. Smith Jr. and Christopher J. Wohl
Langley Research Center, Hampton, Virginia*

*Richard E. Kreeger
Glenn Research Center, Cleveland, Ohio*

*Kevin R. Hadley and Nicholas McDougall
South Dakota School of Mines & Technology, Rapid City, South Dakota*

National Aeronautics and
Space Administration

Langley Research Center
Hampton, Virginia 23681-2199

July 2014

The use of trademarks or names of manufacturers in this report is for accurate reporting and does not constitute an official endorsement, either expressed or implied, of such products or manufacturers by the National Aeronautics and Space Administration.

Available from:

NASA Center for AeroSpace Information
7115 Standard Drive
Hanover, MD 21076-1320
443-757-5802

Hydrogen-Bonding Surfaces for Ice Mitigation

ABSTRACT

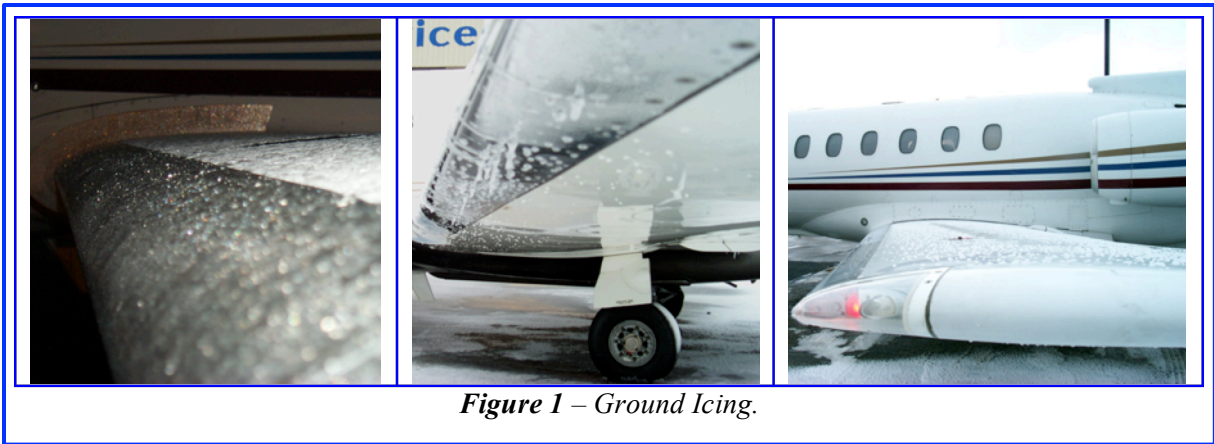
Ice formation on aircraft, either on the ground or in-flight, is a major safety issue. While ground icing events occur predominantly during the winter months, in-flight icing can happen anytime during the year. The latter is more problematic since it could result in increased drag and loss of lift. Under a Phase I ARMD NARI Seedling Activity, coated aluminum surfaces possessing hydrogen-bonding groups were under investigation for mitigating ice formation. Hydroxyl and methyl terminated dimethylethoxysilanes were prepared via known chemistries and characterized by spectroscopic methods. These materials were subsequently used to coat aluminum surfaces. Surface compositions were based on pure hydroxyl and methyl terminated species as well as mixtures of the two. Coated surfaces were characterized by contact angle goniometry. Receding water contact angle data suggested several potential surfaces that may exhibit reduced ice adhesion. Qualitative icing experiments performed under representative environmental temperatures using supercooled distilled water delivered via spray coating were inconclusive. Molecular modeling studies suggested that chain mobility affected the interface between ice and the surface more than terminal group chemical composition. Chain mobility resulted from the creation of “pockets” of increased free volume for longer chains to occupy.

ABBREVIATIONS

A: methyl terminated
AFP: anti-freeze protein
Al: aluminum
ARMD: Aeronautics Research Mission Directorate
CA: contact angle
C#A: methyl terminated carbon chain length of #, where # = 3, 7, 11
C#H: hydroxyl terminated carbon chain length of #, where # = 4, 10, 11
F₄: structure factor
H: hydroxyl terminated
HB: hydrogen-bonding
LAMMPS: Large-scale Atomic /Molecular Massively Parallel Simulator
MD: molecular dynamics
MSD: mean squared diffusion
NARI: NASA Aeronautics Research Institute
Pt/C: platinum on carbon
QLL: quasi-liquid layer
RT: room temperature
SHS: superhydrophobic surfaces
TRL: Technology Readiness Level
TBDS: t-butyldimethylsilyl
VDW: van der Waals

INTRODUCTION

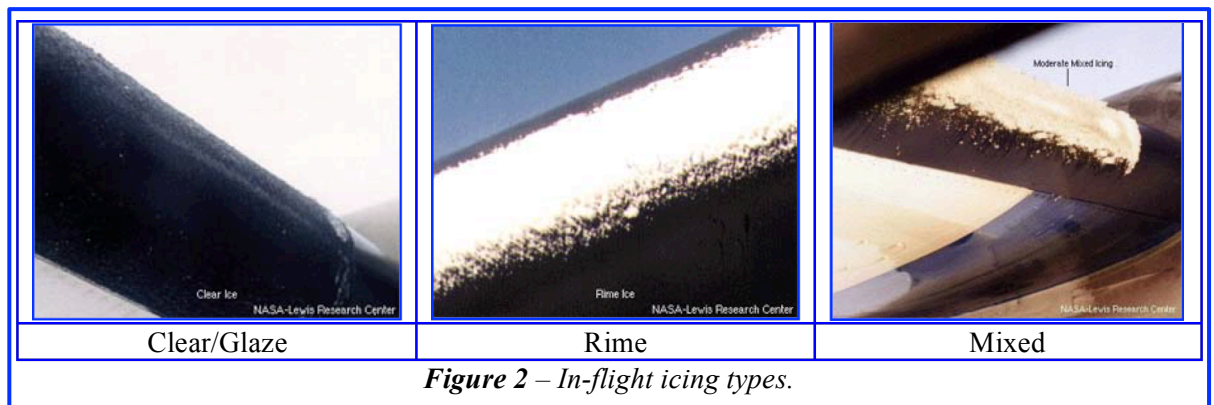
Ice formation on aircraft surfaces affects performance by increasing weight, creating drag, and loss of lift.¹ In general, icing can occur 1) while the aircraft is on the ground prior to take-off at airports in cold regions like Chicago and Minneapolis and 2) while in-flight any time throughout the year.² Ground icing of aircraft, as shown in Figure 1, usually results from freezing conditions that occur during frost, snow



and ice/freezing rain storms. Such events result in coverage of the entire aircraft with impregnation of control surfaces.

Impact icing (i.e. in-flight) occurs when supercooled water droplets impinge and freeze on aircraft surfaces in clouds at temperatures at or below freezing. The term cloud droplet is generally used to describe particles smaller than 0.1 mm in diameter. Typically in nature, median droplet diameters encountered are less than 20 μm . Because of their relatively small size, droplets can exist in a supercooled liquid state in natural clouds down to -20°C , and can be encountered (less frequently) at -30° to -35°C , and even as low as -40°C in the laboratory.³ However, other droplet diameters and size distributions cannot be neglected. Special cases include freezing drizzle, which denotes droplets in the 50-400 μm range, and freezing rain (typically -15° to $+5^{\circ}\text{C}$), which is composed of very large droplets, up to 5 mm in size.

If the droplets freeze on impact, as is the case at temperatures well below freezing, relatively lower speeds and/or lower water contents, the result is rime ice. Rime ice is characterized by a white, opaque, relatively streamlined appearance. At temperatures closer to freezing, higher speeds and/or higher water content, not all the impinging droplets freeze on impact. Some of the impinging water runs along the surface before freezing, a term called runback. This regime results in what is known as glaze ice, typified by a translucent appearance, often exhibiting large hornlike structures. Glaze ice is the most difficult type to detect visually. A parameter known as the freezing fraction helps quantify the two regimes: if the freezing fraction is 1, the ice is rime. If freezing fraction is <1 , the ice is considered glaze. Mixed ice, as the name implies, is a combination of both clear/glaze and rime. Examples of each are shown in Figure 2.



The rate at which impinging water freezes is driven by heat transfer from the aircraft surface, and includes a complicated balance of mechanisms: kinetic heating, convective cooling, latent heat, sensible heat, evaporative cooling. The presence of runback is most likely where surface tension comes into play.

Current strategies used to alleviate icing problems involve pneumatic boots, heated surfaces, and de-icing agents (i.e. ethylene and propylene based glycols).^{4,5} Besides potential environmental concerns,⁶ ground application of de-icing agents can impede efficient throughput of air traffic at airports during the winter months. Thus, a passive rather than active approach is desirable since it would minimize the need of applying de-icing agents (i.e. ground and in-flight) as well as being always responsive to an icing event. Anti-icing coatings are a passive approach that would be applied to the aircraft surface either as a topcoat or as a constituent of aircraft paint. The application frequency for these coatings would ideally conform with routine aircraft maintenance and painting.

Along this line, a number of anti-icing coating strategies have focused on superhydrophobic surfaces (SHS)⁷⁻¹⁰, where the inhibition of ice formation would occur via repulsion of impacting water. However, this repulsion does not prevent frost formation or water from freezing in a humid environment. When this occurs, water is no longer repelled, resulting in potential icing. In addition, the low ice adhesion strengths initially observed with these materials gradually degrade over repeated icing-deicing cycles.

The hypothesis investigated herein involves a more direct anti-icing mechanism: a hydrophilic surface with hydrogen-bonding (HB) capabilities similar to anti-freeze proteins (AFPs) found in certain fish and amphibians.¹¹ This biomimetic approach would result in ice growth inhibition and ice formation prevention via an adsorption mechanism. Figure 3 depicts an AFP possessing HB side-groups (i.e. hydroxyl) strategically located to maximize crystal growth inhibition via adsorption of ice crystals. Antifreeze protection arises from the molecular structure and is known as a constitutive property. In comparison, the addition of a material (e.g. salt) to depress the freezing point is known as a colligative property.¹² The general characteristics of AFPs are:

- thermal hysteresis: reduction in freezing point,
- ice recrystallization inhibition, and
- ice structuring (change in ice crystal morphology)¹²

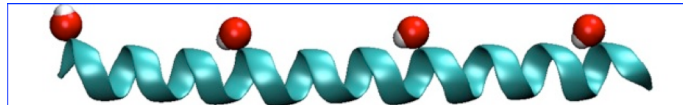


Figure 3 – Type I AFP with regularly spaced alcohol functionality.

Researchers from the Fraunhofer Institute for Manufacturing Technology and Applied Materials Research directly incorporated AFPs from a winter flounder into a coating.¹³ Testing of this material afforded promising results but durability was found to be an issue, presumably due to AFP denaturation which leads to a loss of activity. Thus, generation of a surface with similar morphology to an AFP, but with a more robust matrix, may yield AFP properties while overcoming durability issues. Work performed by Inada's group has shown similar effects with poly(vinyl alcohol), where the alcohol groups bind to the ice crystal via HB and inhibit additional ice growth.¹⁴⁻¹⁸ However, poly(vinyl alcohol) is a poor candidate for surface modification due to its high solubility in water. Anklam and Firoozabadi also demonstrated that HB between water and alcohols contributes to inhibition of crystal growth.¹⁹ Their work highlights how an adsorbed crystal on an inhibitor (e.g. AFP) creates a difference in surface energy between the adsorbed crystal and any further crystal growth. In short, they derived the following relationship for critical growth inhibition:

$$(\Delta\mu)_c = a\Delta\sigma \quad (1)$$

where $\Delta\mu$ is the difference in chemical potential between the old and new crystal, a is the area of contact between the old crystal and the liquid solution, and $\Delta\sigma$ is the difference in surface energy. If $a\Delta\sigma$ is larger than $\Delta\mu$, the thermodynamic driving force to add a new crystal layer cannot overcome the energy or work requirement.

Based on AFP characteristics (i.e. adsorption), this work postulated that direct interaction of water with a HB surface would reorient water molecules, disrupt initial ice nucleation, and induce defect propagation because of the competition between water molecules and a HB surface for HB partners. In contrast to interactions on a SHS, an ice crystal could adsorb to a HB surface, thus lowering the interfacial tension¹⁹ and potentially creating a larger free energy barrier to further ice crystal growth. In addition, a proper HB surface designed for optimal adsorption and interaction has the potential to enhance the quasi-liquid layer (QLL) formed at the surface/ice interface. Specifically, the QLL forms the interface between surfaces and ice crystals. Due to the low temperatures, the water is solid-like. However, because of the presence of a surface, the water cannot form the same type of crystalline network, resulting in the retention of liquid-like properties.^{20,21}

To investigate this hypothesis, aluminum surfaces were coated with 1) methyl and 2) hydroxyl terminated aliphatic alkoxy silanes and 3) a mixture of the two species. Work reported by Petrenko et. al. using pure methyl and hydroxyl terminated C11 aliphatic chain and mixtures of these upon a gold substrate indicated that the hydrophilic surface prepared from the hydroxyl terminated chain exhibited higher ice adhesion strength than the hydrophobic coated surface.²² Additionally, a mixture of the two components (hydroxyl and methyl terminated C11 chains) provided a linear relationship with respect to ice shear strength that increased with increasing hydroxyl component. These surfaces were molecularly smooth due to similar chain lengths of the two materials.

Dai and Evans performed molecular dynamic (MD) simulations on alcohol-terminated monolayers to investigate how monolayers of uniform length promote ice growth.²³ Their studies showed that alcohols arranged in a specific way can initiate a “template” for new ice crystal formation, which catalyzed crystal growth on the surface. The authors found an odd-number of carbons in the surface modifier alkyl chain enabled better exposure of the alcohol to the water molecules, minimized surface roughness, and served as a better initial template for crystal growth. Roughness was defined as the average deviation of the oxygen’s distance to a reference plane. With even-numbered modifiers, the tilting of the alcohol group results in surfaces that do not serve as good templates for ice growth and that exhibit greater surface roughness. Although the exposure is a contributing factor, the authors emphasized that a smooth surface is necessary for growth promotion, as suggested by Petrenko et.al.²² Thus a molecularly rough surface should disrupt ice growth.

Since AFPs are not considered molecularly smooth surfaces, it was of interest to investigate the effect of chain length (i.e. aliphatic spacer between the chain terminus and the substrate surface) of these three material compositions described above upon ice formation. Presumably the difference in chain length would afford molecular (Ångstrom scale) surface roughness that would effectively reduce ice formation and adherence akin to AFPs. In addition, a molecularly rough surface would have two beneficial effects regarding anti-icing: First, the difference in chain length would create “pockets” on the surface where water molecules could adsorb, leaving behind fewer water molecules to form a good HB network in ice and in the QLL. These pockets would be located above the short chains ends and between the extra carbons of the long chains. The pockets would also create more free volume for the chains to move and deform, thus physically disrupting the water molecules near the surface. MD simulations were conducted to test these ideas and to provide an understanding of the effect these surfaces have upon icing. Specifically, the simulations provided a molecular level insight into the formation and growth of the QLL, as opposed to ice, taking into account surface functionality and roughness.

Experimental

A. Materials and Methods

Propyldimethylmethoxysilane (C3A) and t-butyltrimethylchlorosilane [2.85 M (48-52%) in toluene] were purchased from Gelest Inc. and used as received. Tetrabutylammonium fluoride, dimethylethoxysilane, 3-buten-1-ol, 1-heptene, 1-undecene, 9-decen-1-ol, 10-undecene-1-ol, and 10% platinum on carbon (Pt/C) were purchased from Sigma-Aldrich and used as-received. Aluminum (Al) 6061 alloy sheets were purchased from Grainger. Other materials were obtained from commercial sources and used as received. Infrared spectroscopy was performed on liquids using a Thermo-Nicolet IR300 using an ATR accessory. Proton (^1H), carbon (^{13}C), and silicon (^{29}Si) NMR were performed on a Bruker 300 multinuclear FT-NMR spectrometer in deuterated chloroform. Material structures and coating compositions are designated in Table 1. C#A and C#H denote the methyl (A) and hydroxyl (H) terminated species, respectively, where # is the number of carbons in the aliphatic chain. For the C#A molecules, the chain terminating carbon is included, while for H it designates the number of carbons between silicon and the hydroxyl endgroup.

B. Methyl terminated dimethylmethoxysilanes (C7A and C11A)

Into a flame dried single-necked 250 mL single-neck round-bottom flask fitted with a magnetic stir bar was charged the appropriate vinyl terminated n-alkane (1-heptene or 1-undecene) and 10% Pt/C. Dimethylethoxysilane was then added and the mix allowed to stir overnight under ambient conditions. The reaction mixture was then diluted with hexanes and filtered using Celite[®] 545 to remove the 10% Pt/C catalyst. The solvent was removed in vacuo to afford the product in approximate 80% yield. The product was determined by spectral analysis to be of sufficient purity for use in coating Al substrates as described in D.2.

C7A: 77% yield, light yellow liquid. ^1H NMR (ppm): 3.57 (q, 2H, $\text{CH}_3\text{-CH}_2\text{-O-Si}$), 1.20 (s, 10H, $-\text{CH}_2-$), 1.10 (t, 3H, $\text{Si-O-CH}_2\text{-CH}_3$), 0.79 (t, 3H, $-\text{CH}_2\text{-CH}_3$), 0.50 (q, 2H, $\text{Si-CH}_2\text{-CH}_2-$), 0.0 (s, 6H, $(\text{CH}_3)_2\text{-Si}$). ^{13}C NMR (ppm): 60.31, 35.57, 33.93, 31.17, 25.33, 24.83, 20.69, 18.48, 16.19, 0.02. ^{29}Si (ppm): 17.35. FTIR (cm^{-1}): 2933, 2921, 2853, 1455, 1390, 1249, 1106, 1076, 942, 830, 775.

C11A: 82% yield, straw colored liquid. ^1H NMR (ppm): 3.58 (q, 2H, $\text{CH}_3\text{-CH}_2\text{-O-Si}$), 1.17 (s, 18H, $-\text{CH}_2-$), 1.09 (t, 3H, $\text{Si-O-CH}_2\text{-CH}_3$), 0.79 (t, 3H, $-\text{CH}_2\text{-CH}_3$), 0.50 (q, 2H, $\text{Si-CH}_2\text{-CH}_2-$), 0.0 (s, 6H, $(\text{CH}_3)_2\text{-Si}$). ^{13}C NMR (ppm): 58.16, 33.61, 32.00, 29.72, 29.65, 29.60, 29.37, 23.20, 22.69, 18.57, 16.37, 14.10, -2.10. ^{29}Si (ppm): 17.31. FTIR (cm^{-1}): 2939, 2922, 2853, 1457, 1388, 1250, 1107, 1076, 943, 835, 780.

C. TBDS protected dimethylmethoxysilanes (C4TBDS, C10TBDS, and C11TBDS)

1. t-butyltrimethylsilyl (TBDS) protected vinyl alcohols

The procedure was based upon that described in reference 24. Into a flame dried three-necked 100 mL round-bottom flask fitted with a magnetic stir bar, nitrogen inlet, and drying tube containing Drierite[™] was charged the appropriate vinyl alcohol (3-buten-1-ol, 9-decen-1-ol, or 10-undecene-1-ol), dimethylformamide, and imidazole. Once dissolved, t-butyltrimethylchlorosilane in toluene was added via an addition funnel to the stirred mixture. After addition, the flask immediately became warm and returned to room temperature (RT) after approximately 15 min. During this time the solution turned cloudy. The mixture was stirred at RT under nitrogen overnight. Water was then added to destroy residual t-butyltrimethylchlorosilane and solubilize the salts. The mixture was transferred to a separatory funnel and the organic layer recovered. The aqueous layer was extracted with ethyl acetate and the washings combined with the organic layer. The organic layer was then dried over magnesium sulfate. The magnesium sulfate was removed via filtration. The solvent was removed in vacuo to afford the product. The product was determined by spectral analysis to be of sufficient purity for use in C.2.

3-buten-1-O-TBDS: 41% yield. ^1H NMR (ppm): 5.76 (m, 1H, $\text{H}_2\text{C}=\text{CH}-$), 5.01 (t, 2H, $\text{H}_2\text{C}=\text{CH}-$), 3.60 (t, 2H, $-\text{CH}_2-\text{O}-$), 2.22 (q, 2H, $\text{H}_2\text{C}=\text{CH}-\text{CH}_2-$), 0.85 (s, 9H, $(\text{CH}_3)_3\text{-C-Si}$), 0.0 (s, 6H, $(\text{CH}_3)_2\text{-Si}$). ^{13}C NMR (ppm): 135.45, 116.35, 62.90, 37.56, 26.00, 18.39, -5.19. ^{29}Si (ppm): 18.88. FTIR (cm^{-1}): 3071, 2933, 2927, 2868, 2855, 1471, 1254, 1093, 907, 832, 773.

9-decen-1-O-TBDS: 54% yield, clear liquid. ^1H NMR (ppm): 5.75 (m, 1H, $\text{H}_2\text{C}=\text{CH}-$), 4.92 (m, 2H, $\text{H}_2\text{C}=\text{CH}-$), 3.56 (t, 2H, $-\text{CH}_2-\text{O}-$), 1.99 (q, 2H, $\text{H}_2\text{C}=\text{CH}-\text{CH}_2-$), 1.46 (m, 2H, $-\text{CH}_2-$), 1.25 (s, 10H, $-\text{CH}_2-$), 0.85 (s, 9H, $(\text{CH}_3)_3\text{-C-Si}$), 0.0 (s, 6H, $(\text{CH}_3)_2\text{-Si}$). ^{13}C NMR (ppm): 139.21, 114.11, 63.35, 33.80, 32.8, 29.48, 29.39, 29.09, 28.93, 25.98, 25.79, 18.35, -5.28. ^{29}Si (ppm): 18.26. FTIR (cm^{-1}): 3062, 2925, 2854, 1462, 1253, 1095, 907, 832, 772.

10-undecene-1-O-TBDS: 58% yield, clear liquid. ^1H NMR (ppm): 5.81 (m, 1H, $\text{H}_2\text{C}=\text{CH}-$), 4.88 (m, 2H, $\text{H}_2\text{C}=\text{CH}-$), 3.55 (t, 2H, $-\text{CH}_2-\text{O}-$), 2.05 (q, 2H, $\text{H}_2\text{C}=\text{CH}-\text{CH}_2-$), 1.45 (m, 2H, $-\text{CH}_2-$), 1.33 (s, 12H, $-\text{CH}_2-$), 0.85 (s, 9H, $(\text{CH}_3)_3\text{-C-Si}$), 0.0 (s, 6H, $(\text{CH}_3)_2\text{-Si}$). ^{13}C NMR (ppm): 139.18, 114.11, 63.32, 33.86, 32.91, 29.60, 29.46, 29.15, 28.97, 25.98, 25.81, 18.37, -5.27. ^{29}Si (ppm): not obtained. FTIR (cm^{-1}): 3061, 2925, 2856, 1462, 1252, 1095, 908, 834, 772.

2. TBDS protected dimethylethoxysilanes

Into a flame dried single-necked 100 mL round-bottom flask fitted with a magnetic stir bar was charged the appropriate TBDS protected vinyl alcohol (prepared in C.1) and 10% Pt/C. Dimethylethoxysilane was added and the mix allowed to stir overnight under ambient conditions. The reaction mixture was diluted with toluene and filtered to remove the 10% Pt/C catalyst. The solvent was removed in vacuo followed by heating under vacuum at approximately 50°C to afford the product in approximate 90% yield. The product was determined by spectral analysis to be of sufficient purity for use in coating Al substrates as described in D.2.

C4TBDS: 90% yield, amber liquid. ^1H NMR (ppm): 3.60 (m, 2H, $-\text{CH}_2-\text{O}-$), 1.51 (q, 2H, $\text{Si-CH}_2-\text{CH}_2-$), 1.36 (q, 2H, $\text{Si-CH}_2-\text{CH}_2-$), 1.14 (t, 3H, $\text{Si-CH}_2-\text{CH}_3$), 0.85 (s, 9H, $(\text{CH}_3)_3\text{-C-Si}$), 0.55 (q, 2H, $\text{Si-CH}_2-\text{CH}_3$), 0.05 (s, 6H, $(\text{CH}_3)_2\text{-Si}$), 0.0 (s, 6H, $(\text{CH}_3)_2\text{-Si}$). ^{13}C NMR (ppm): 62.80, 58.19, 36.43, 25.96, 19.43, 18.56, 18.32, 18.07, -2.11, -5.28. ^{29}Si (ppm): 18.32, 17.26. FTIR (cm^{-1}): 2934, 2927, 2869, 2856, 1471, 1388, 1250, 1097, 938, 831, 773.

C10TBDS: 87% yield, yellow liquid. ^1H NMR (ppm): 3.63 (m, 2H, $\text{CH}_3-\text{CH}_2-\text{O-Si}$), 3.55 (m, 2H, $-\text{CH}_2-\text{CH}_2-\text{O-Si}$), 1.47 (m, 2H, $-\text{CH}_2-$), 1.23 (s, 14H, $-\text{CH}_2-$), 1.14 (t, 3H, $\text{Si-CH}_2-\text{CH}_3$), 0.85 (s, 9H, $(\text{CH}_3)_3\text{-C-Si}$), 0.55 (q, 2H, $\text{Si-CH}_2-\text{CH}_2-$), 0.05 (s, 6H, $(\text{CH}_3)_2\text{-Si}$), 0.0 (s, 6H, $(\text{CH}_3)_2\text{-Si}$). ^{13}C NMR (ppm): 61.64, 56.48, 31.80, 31.19, 27.97, 27.82, 27.77, 27.64, 24.29, 24.11, 21.49, 16.88, 16.68, 14.68, -3.78, -6.96. ^{29}Si (ppm): 18.30, 17.30. FTIR (cm^{-1}): 2942, 2924, 1462, 1388, 1249, 1099, 937, 831, 774.

C11TBDS: 89% yield, yellow liquid. ^1H NMR (ppm): 3.62 (m, 2H, $\text{CH}_3-\text{CH}_2-\text{O-Si}$), 3.55 (m, 2H, $-\text{CH}_2-\text{CH}_2-\text{O-Si}$), 1.46 (m, 2H, $-\text{CH}_2-$), 1.24 (s, 16H, $-\text{CH}_2-$), 1.14 (t, 3H, $\text{Si-CH}_2-\text{CH}_3$), 0.85 (s, 9H, $(\text{CH}_3)_3\text{-C-Si}$), 0.55 (q, 2H, $\text{Si-CH}_2-\text{CH}_2-$), 0.05 (s, 6H, $(\text{CH}_3)_2\text{-Si}$), 0.0 (s, 6H, $(\text{CH}_3)_2\text{-Si}$). ^{13}C NMR (ppm): 63.29, 58.14, 33.47, 32.88, 29.63, 29.55, 29.44, 29.34, 25.96, 25.81, 23.19, 18.56, 18.35, 16.36, 0.38, -2.09, -5.27. ^{29}Si (ppm): 18.25, 17.25. FTIR (cm^{-1}): 2942, 2923, 2853, 1461, 1387, 1249, 1099, 938, 831, 774.

D. Al Alloy Surfaces

1. Preparation

Al plates (approximate 30.5 cm x 30.5 cm) were cut into squares (2.54 cm x 2.54 cm), circles (2.54 cm diameter), and rectangles (10.2 cm x 7.6 cm) using a water jet. The Al specimens were subsequently cleaned, degreased, dried, and wrapped in brown paper prior to use. Surface roughness measurements

were collected on a FRT of America MicroProf 100. The measurement size was 1 cm square with data collected at 2000 points per line and 200 lines, which equates to 5 μm between data points and 50 μm between lines. Thus, the arithmetic average roughness (R_a) and root-mean-square roughness (R_q) for the as-cleaned substrates were 0.249 and 0.313 μm , respectively. After polishing these values decreased to 0.018 and 0.022 μm , respectively.

2. Deposition of substituted dimethylalkoxysilanes

To a vial containing approximately 0.3 g of the appropriate substituted dimethylalkoxysilane(s), a mixture of ethanol:water:methylene chloride (82:6:12) was added to afford an approximate 2% (w/v) solution. Several drops of glacial acetic acid were added to the mixture to generate the corresponding silanol. The pH ranged from 4.5 to 5.5. The mixture was agitated on a shaker for approximately 0.5 h at RT prior to deposition on the Al substrate via spray coating. Spray coating was performed using a Badger 250-2 basic spray gun. The coated samples were allowed to stand at RT in air overnight and then placed in an air oven at approximately 110°C for 15 min.

3. TBDS deprotection

The coatings on Al generated from TBDS protected dimethylmethoxysilanes (C4TBDS, C10TBDS, C11TBDS) were soaked in a tetrabutylammonium fluoride solution (approximately 0.0055 M in tetrahydrofuran) at RT for approximately 72 h. The specimens were subsequently removed, rinsed with distilled water, and air-dried at RT.

E. Contact Angle Goniometry

A First Ten Angstroms FTA 1000B goniometer was used to obtain contact angle data at ambient conditions. Contact angles were measured for each sample using an 8 μL drop of either water or ethylene glycol or a 2 μL drop of methylene iodide. Tilting axis measurements were utilized to measure sessile, advancing, and receding contact angles. For each liquid, interfacial tension measurements were made of a suspended drop prior to experimentation to verify liquid purity and precision of the focused image. Contact angles were determined by drop shape analysis.

F. Qualitative Icing Experiment

Samples (approximate 7.6 cm x 10.2 cm) were attached to plate glass with double sided tape and placed in a ScienTemp™ 34-07 Moderate Cold Freezer at test temperature approximately 24 h prior to spray coating with supercooled distilled water. Test temperatures were -10, -15, and -20°C. Supercooled distilled water was prepared by placing an Erlenmeyer flask containing distilled water into an ice-water-salt bath for at least 4 h prior to use. The temperature of the bath was approximately -4°C. The temperature of the supercooled water was approximately -0.1°C prior to spraying. The supercooled distilled water was added to a 60 mL spray jar and used to spray coat pre-cooled test panels inside the freezer using a Badger 250-2 basic spray gun. Samples were then allowed to stand undisturbed at freezer conditions overnight prior to visual observation.

G. Freezing Point Determination of Water

1. Ice formation stage

Determination of the temperature at which water microdroplets freeze on a surface was determined using a custom-built temperature-controlled stage. The temperature was controlled by adjusting the relative amount of heated or cooled gaseous nitrogen supplied to a cavity under the sample. Temperature controlling was achieved using a logic gate system that derived commands from an Omega CN3000 temperature controller. The logic gates controllably adjust two channels that supply the heated and cooled nitrogen. Nitrogen was delivered using a low pressure (414 MPa) house nitrogen line. The nitrogen passed through a Domnick Hunter air dryer followed by a drying tube. This line then split to feed the heated and cooled gas lines. Nitrogen was heated by wrapping the copper tubing with a heating element

set to 232°C. Nitrogen was cooled by submerging coiled copper tubing, through which the gas flowed, into liquid nitrogen. Both lines recombined prior to the sample stage, which was fabricated from a solid piece of polytetrafluoroethylene (PTFE). The PTFE block had two exit ports for the nitrogen, both of which were outfitted with thermocouples. One thermocouple measured the gas temperature while the other measured sample temperature. The sample used for these experiments was a 2.54 cm Al disc. This disc was placed in the PTFE block above the gas delivery chamber. A rubber o-ring, with a thin application of vacuum grease, was placed on top of the sample, followed by a cover slip. On top of this, a digital microscope (Dino-Lite Pro) was positioned and held with enough pressure to ensure an air-tight seal between the sample and cover slip. Images were captured as deemed appropriate to identify the various stages of microdroplet formation and freezing on the sample surface.

2. Microdroplet freezing experiment

Prior to placing the cover slip on top of the rubber o-ring, water (0.5-5 μL) was deposited on the sample surface using a micropipette or syringe. Upon replacement of the coverslip and microscope, the temperature controller was adjusted to approximately 88°C. Water vaporization was visualized on the optical microscope image (approximately 210X) as a rapid transition from a transparent to opaque cover slip surface. Once the visual region was fully covered with water vapor, the temperature controller was set to 4°C to induce condensation of microdroplets on the sample surface. Once the microdroplets were deposited, the temperature controller was adjusted to -23°C and the temperature at which the microdroplets froze (observed as a change in the opacity of the microdroplets as well as an increase in angularity of the microdroplet edges) was recorded. Changes in both gas and stage temperature were recorded using a 3-Channel Extech Datalogger.

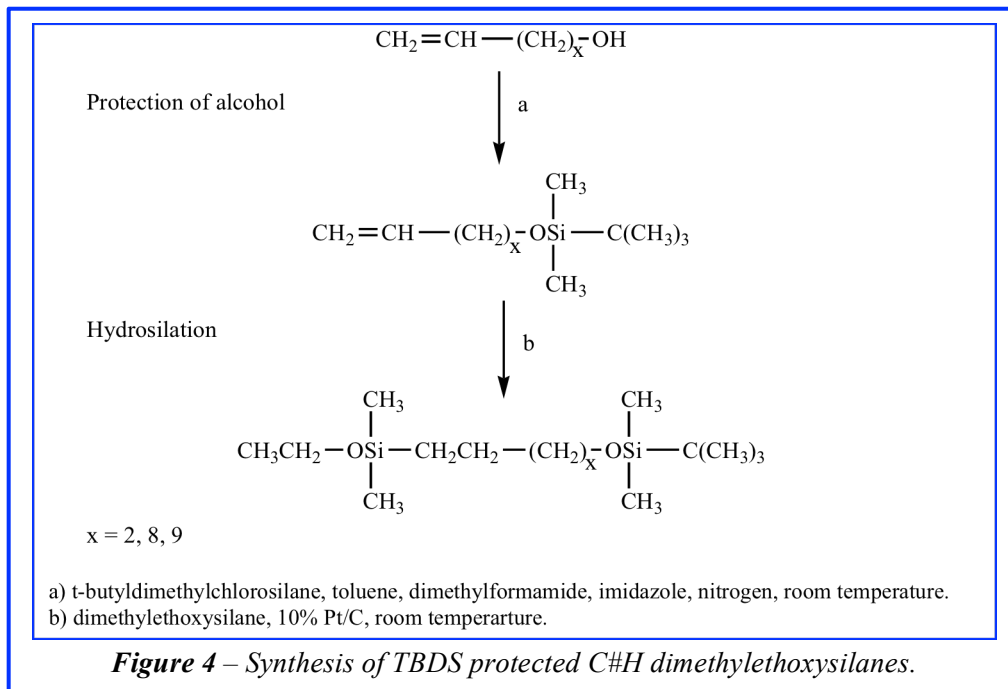
H. MD Simulations

Simulations were run using the open source code LAMMPS (Large-scale Atomic /Molecular Massively Parallel Simulator).²⁵ Surfaces were modeled as the surface modifier (aliphatic chains of various lengths and various terminal carbon chemical compositions) bonded to silica. All simulations were modeled with the Nosé-Hoover thermostat²⁶ to maintain temperature in a constant number of molecules, volume, and temperature (NVT) ensemble at 230 K (-43°C). These simulations used the same temperature so deformation was not biased due to temperature effects. Periodic boundary conditions were applied parallel to the surface rather than normal to it so that the backside of the ice crystal would be exposed to a vacuum rather than another surface. To systematically study the effects of different surface modifiers, heuristics were developed for building the model and running the simulations. The surface modifier and silica utilized a combination of the Dreiding force field²⁷ (for carbon backbones and silica substrate) and the Charmm General Force Field (CGenFF)²⁸ for the HB functional groups. Water molecules (3360) were placed on a lattice matching an ice crystal in the wurtzite hexagonal phase, ice-Ih. The TIP4PQ/2005¹³ model was then used since it produced the most accurate simulated ice structures compared to experiments.^{29,30} Once a proper interface was established, the simulation was run for an additional 2.0 ns.

Results and Discussion

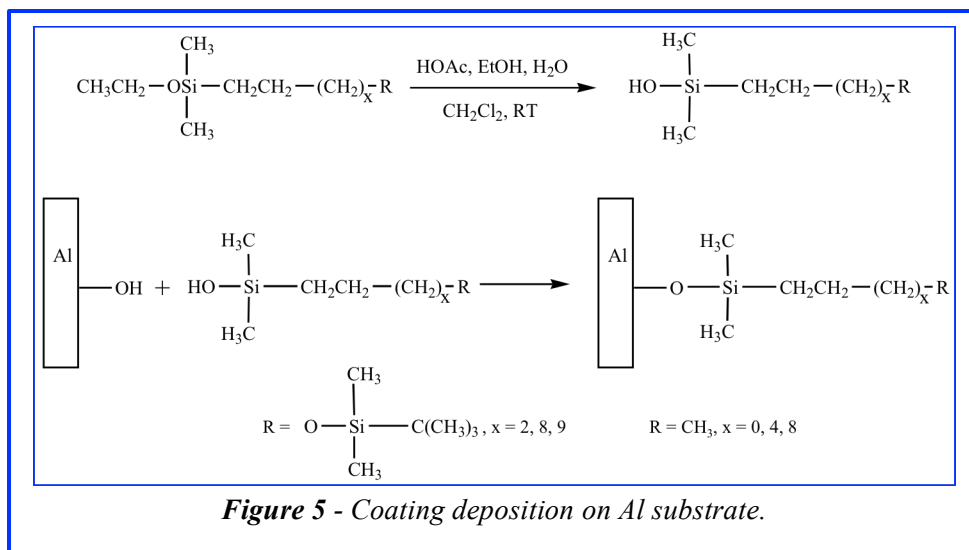
Material Preparation

Hydroxyl terminated alkoxy silanes were prepared as shown in Figure 4. Since the silanol group (generated from the parent alkoxy silane during deposition of the modifier to the Al substrate) had the potential to condense with the hydroxyl group, the vinyl alcohol needed to be protected. A number of moieties are available to protect the hydroxyl group.^{31,32} After review of the literature, the t-butyl dimethylsilyl (TBDS) group was selected based on its stability to a number of reaction conditions that were to be employed as well as its suggested ease of removal. The protected vinyl-alcohols were prepared in approximately 40-60% yield from TBDS chloride and the parent vinyl alcohol with the structures confirmed by NMR and IR spectroscopies.



Originally it was proposed that 1) HB/non-HB modifiers were to be functionalized with trialkoxysilane endgroups and 2) HB modifiers were to have carbon chain lengths (C) of 2, 3, 10, and 11. Regarding material termination with the trialkoxysilane group, it was determined that a monoalkoxysilane endgroup would be preferable since it would ensure that unreacted silanol groups would not be present after deposition on the substrate. For HB modifiers where $C = 2$ and 3, difficulties were encountered with hydrosilation of the protected vinyl alcohols. A literature review suggested these materials were plagued by side reaction affording low product yields.^{33,34} Consequently these two materials were dropped from consideration and substituted with a four carbon chain ($x=2$, Figure 4). Hydrosilation of the vinyl TBDS protected alcohols with dimethylethoxysilane in the presence of a Pt/C catalyst afforded TBDS protected HB modifiers in approximately 90% yield. Aliphatic analogs C7A and C11A were not available commercially and were prepared from the vinyl terminated precursors under similar conditions as the C#H compounds. Material structures were confirmed by NMR (^1H , ^{13}C , ^{29}Si) and ATR-FTIR spectroscopies. The disappearance of the peak in the FTIR spectra at approximately 3060 cm^{-1} , corresponding to the vinyl stretch, and at approximately 5.8 and 5.0 ppm in the ^1H NMR spectra, indicated that the hydrosilation reaction had proceeded to completion.³⁵ Based on NMR spectroscopy, the compounds were determined to be of sufficient purity to coat the Al substrate. No attempt was made to optimize reaction conditions to maximize product yields.

Specimens sized for contact angle (CA) analysis and in-house qualitative icing experiments were cut from Al 6061 plates via water-jet, cleaned, and degreased. Deposition of the appropriate surface modifier(s) on the Al substrate was performed by spray coating an approximate 2% (w/v) aqueous ethanol - methylene chloride mixture that was acidified with glacial acetic acid (Figure 5) with compositions listed in Table 1. The condensation reaction was allowed to proceed at ambient conditions overnight followed by a 15 min thermal cure at 110°C .



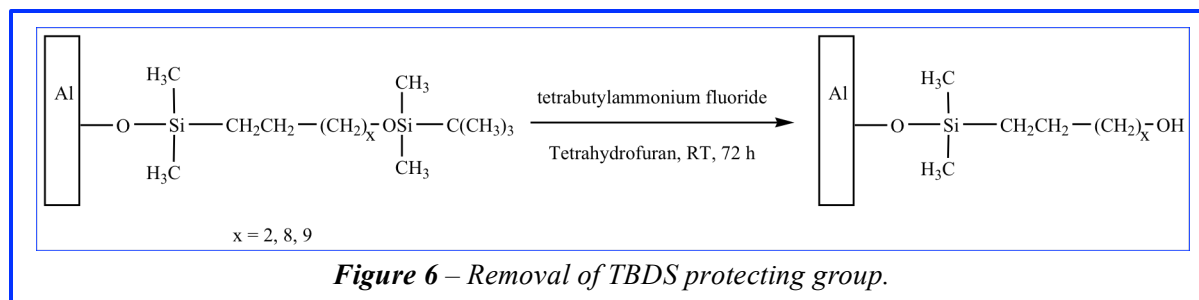
The TBDS protected HB modifiers (C#H) required removal of the protecting group after the deposition process to regenerate the hydroxyl species. In the literature the following conditions were reported to remove the TBDS protecting group: 1) methanol/1% hydrochloric acid³⁶, 2) glacial acetic acid/ water (2:1)³², and 3) tetrabutylammonium fluoride in tetrahydrofuran.²⁴ Even though the TBDS group was reported to be easy to remove, it was found that the conditions were ineffective as determined by CA analysis with water. Possible reasons for this inability to remove TBDS may be 1) reactions are carried out in a homogeneous solution or 2) the material being exposed to a standing solution. Since the TBDS protected HB modifiers were attached to the substrate, they may or may not be solubilized in the deprotection solution. Initially a short exposure time to tetrabutylammonium fluoride in tetrahydrofuran at RT was found to be ineffective; however, a 72 h exposure resulted in the removal of the TBDS protecting

Table 1 - Coating Compositions

Aliphatic (A)	Hydroxy (H)	Hydroxy/Aliphatic (H/A)
100% C3A	100% C4H	50% C4H/50% C3A
100% C7A	100% C10H	50% C4H/50% C7A
100% C11A	100% C11H	25% C10H/75% C7A
25% C11A/75% C3A	50% C4H/50% C10H	50% C10H/50% C7A
50% C11A/50% C3A	50% C4H/50% C11H	75% C10H/25% C7A
75% C11A/25% C3A	50% C10H/50% C11H	50% C11H/50% C11A
50% C11A/50% C7A		

$$\begin{array}{c}
 \text{Al}-\text{O}-\text{Si}(\text{CH}_3)_2-\text{CH}_2\text{CH}_2-(\text{CH}_2)_x-\text{R}
 \end{array}$$

A: R = CH₃, x = 0 (C3A), 4 (C7A), 8 (C11A)
H: R = OH, x = 2 (C4H), 8 (C10H), 9 (C11H)



group from the HB modifiers (Figure 6) affording the corresponding hydroxyl terminated structure as determined from water sessile drops by CA goniometry. The sessile water CA for the protected C10H and C11H modifiers was 101.0° and 108.0°, respectively, and after deprotection was 74.9° and 69.6°, respectively.

Surface Characterization

All compositions were characterized by tilting angle CA goniometry using water, ethylene glycol, and methylene iodide. Data obtained for sessile, receding, and advancing CAs is presented in Table 2.

To determine the specific intermolecular contributions [dispersive (γ^d) and polar (γ^p)] of the surface energies for each of the surfaces, the regression line analysis method developed by Kaelble³⁷ was used. The CA data in Table 2 for the sessile, receding, and advancing CAs was used to determine the

Table 2 - Contact Angle per Sample Composition

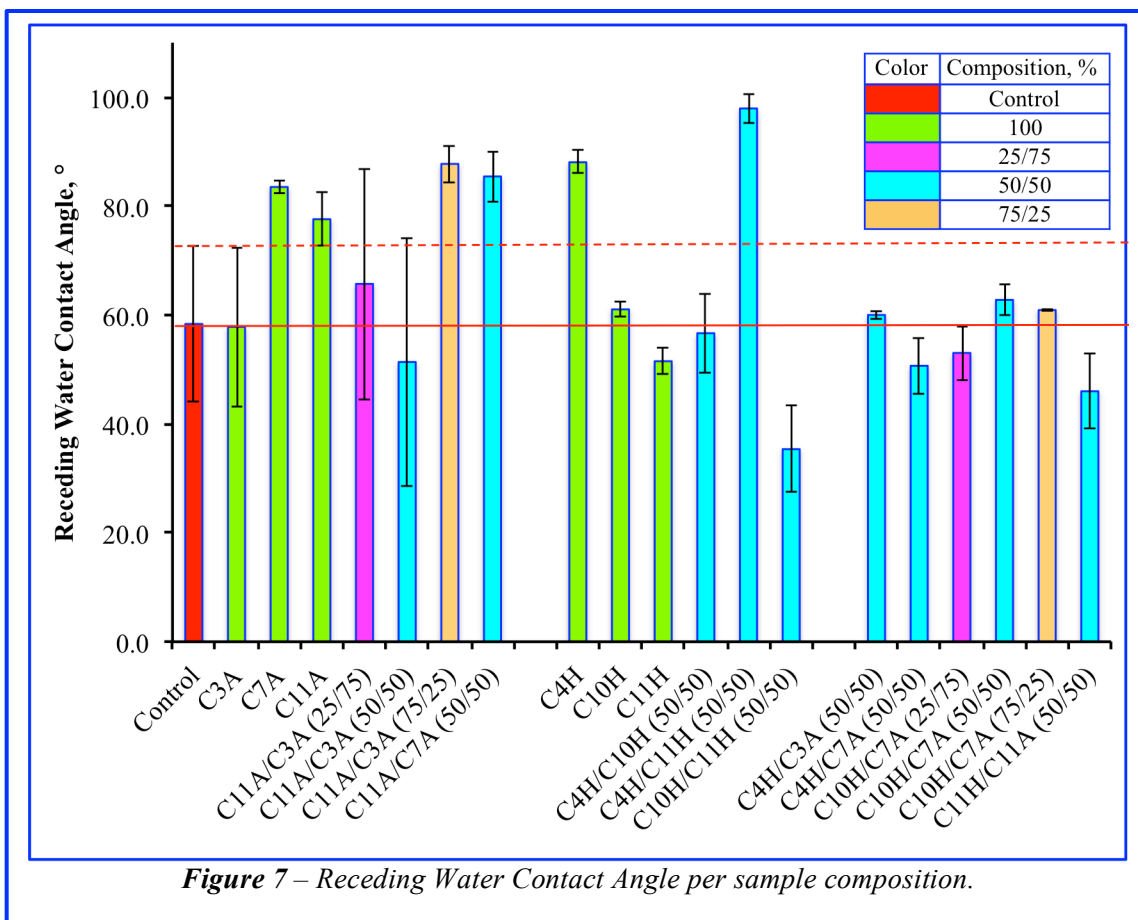
Composition	Contact Angle, °								
	Water			Ethylene Glycol			Methylene Iodide		
	θ_s	θ_a	θ_r	θ_s	θ_a	θ_r	θ_s	θ_a	θ_r
Al Control	72.7	76.2	58.4	63.8	67.3	34.4	65.7	73.2	30.7
Aliphatic									
C3A	69.9	72.7	57.8	62.3	66.0	32.7	55.3	62.8	14.9
C7A	102.1	104.2	83.5	76.9	79.2	45.2	60.3	65	32.2
C11A	92.9	94.4	77.6	78.6	80.7	54.1	65.9	67.5	21.6
C11A/C3A (25/75)	84.1	85.7	65.7	51.5	60.2	26.2	57.1	63.4	21.0
C11A/C3A (50/50)	63.2	67.7	51.4	63.8	70.3	39.1	65.1	71.4	27.0
C11A/C3A (75/25)	105.0	108.7	87.7	71.9	78.5	46.9	65.6	69.8	22.9
C11A/C7A (50/50)	101.7	102.6	85.4	81.3	80.2	51.0	68.0	71.3	18.0
Hydroxy									
C4H	108.3	106.9	88.0	45.4	51.4	24.6	60.3	65.0	32.2
C10H	74.9	77.5	61.0	55.9	61.0	23.2	50.7	53.4	13.5
C11H	69.6	71.2	51.5	61.4	64.5	30.6	51.1	61.2	14.1
C4H/C10H (50/50)	72.2	74.5	56.7	42.9	51.5	21.3	45.5	47.2	12.5
C4H/C11H (50/50)	118.4	122.1	97.9	57.2	63.3	30.1	49.3	51.8	12.3
C10H/C11H (50/50)	42.2	60.3	35.4	35.5	52.0	16.0	41.0	42.5	14.0
Hydroxy/Aliphatic									
C4H/C3A (50/50)	74.7	78.2	60.0	56.1	60.8	24.9	52.5	63.2	13.8
C4H/C7A (50/50)	67.0	72.0	50.7	52.5	63.9	23.1	49.2	55.4	13.5
C10H/C7A (25/75)	64.3	71.2	53.0	59.2	62.4	27.5	48.1	54.9	12.6
C10H/C7A (50/50)	75.8	80.5	62.8	58.0	62.0	27.3	53.3	60.7	14.0
C10H/C7A (75/25)	75.3	80.0	60.9	60.4	64.2	27.4	44.0	58.0	12.8
C11H/C11A(50/50)	66.5	74.2	46.0	62.1	67.0	34.8	49.2	54.9	11.5

corresponding surface energies with the results reported in Table 3. In general, surface energies of the compositions were greater than the control with the exception of several C11 compositions. Results obtained for the C3A and C4H surfaces were not consistent with other A and H surfaces, respectively, that had a longer aliphatic spacer between the surface and chain termini. Regarding the C3A surface, one explanation is that water is able to interact with the Al surface due to the short chain length. Water penetration depths calculated from MD simulation work discussed later suggested that this interaction was plausible. The result for the C4H surface may be associated with the short chain length as well as the TBDS protecting group that was present during deposition of the material. This could have resulted in lower material coverage due to steric crowding of the TBDS groups. Upon removal of the TBDS group, the newly generated hydroxyl substituent could have HB with hydroxyl moieties present on the Al surface, thus affording a nonpolar surface due to the aliphatic backbone being exposed. A similar situation can be envisioned for the C4H/C11H (50/50) composition. Here the hydroxyl groups of C11H could HB with the C4H hydroxyl groups, generating a nonpolar surface.

Meuler et. al. reported that for relatively smooth surfaces, receding water CAs could be used to predict icephobicity, where a high receding CA relates to lower ice adhesion strength.³⁸ Based on this report, the receding water CA data shown in Table 2 for the various compositions were compared to the Al control (Figure 7). The dashed and solid lines signify the upper bound of the standard deviation and average value, respectively, for the control. The following compositions would be anticipated to exhibit lower ice adhesion strengths than the control based upon the dashed line: C7A, C11A, C11A/C3A (75/25), C11A/C7A (50/50), C4H, and C4H/C11H (50/50). Using the solid line, other compositions of interest are C11A/C3A (25/75), C10H, C10H/C7A (50/50, 75/25), and C4H/C3A (50/50).

Table 3 - Surface Energy per Sample Composition

Composition	Surface Energy, mJ/m ²								
	Sessile			Advancing			Receding		
	γ^D	γ^P	γ^{Tot}	γ^D	γ^P	γ^{Tot}	γ^D	γ^P	γ^{Tot}
Al Control	10.8	21.4	32.2	18.1	10.8	28.8	38.8	11.6	50.4
Aliphatic									
C3A	25.8	9.9	35.7	22.2	10.1	32.3	43.1	10.2	53.3
C7A	27.4	0.3	27.7	25.0	0.3	25.3	42.9	1.9	44.8
C11A	22.3	2.4	24.7	21.4	2.1	23.6	42.3	2.8	45.1
C11A/C3A (25/75)	30.6	4.1	34.7	26.0	4.4	30.4	44.9	7.2	52.0
C11A/C3A (50/50)	19.8	16.3	36.1	16.7	15.3	32.0	37.5	14.6	52.1
C11A/C3A (75/25)	26.7	0.2	26.9	23.8	0.1	24.0	46.8	0.7	47.5
C11A/C7A (50/50)	0.7	22.6	23.3	21.5	0.8	22.3	46.3	0.9	47.2
Hydroxy									
C4H	36.4	0.0	36.4	32.2	0.1	32.3	48.1	1.0	49.1
C10H	30.4	6.7	37.1	28.6	6.0	34.6	45.6	8.7	54.3
C11H	27.7	9.2	37.0	22.9	10.5	33.5	42.0	13.2	55.3
C4H/C10H (50/50)	34.8	7.2	42.0	32.8	6.4	39.2	44.9	10.6	55.5
C4H/C11H (50/50)	42.2	1.3	43.4	40.1	1.8	41.9	56.2	0.03	56.2
C10H/C11H (50/50)	31.5	22.4	53.9	31.4	12.4	43.8	40.7	21.2	61.9
Hydroxy/Aliphatic									
C4H/C3A (50/50)	29.5	7.1	36.6	24.3	7.5	31.8	45.0	9.2	54.2
C4H/C7A (50/50)	29.9	10.3	40.2	25.8	8.9	34.7	43.0	13.6	56.7
C10H/C7A (25/75)	28.3	11.4	39.7	26.2	9.2	35.4	43.1	12.4	55.5
C10H/C7A (50/50)	28.9	6.8	35.7	25.7	6.0	31.7	45.4	7.9	53.3
C10H/C7A (75/25)	32.4	5.5	37.9	26.4	5.7	32.1	45.1	8.7	53.8
C11H/C11A(50/50)	27.7	10.4	38.1	25.8	7.7	33.5	40.5	15.8	56.3



Another means of comparing these surfaces was by a plot of the polar component vs. the disperse component of the surface energy of the surface of interest. This plot, known as a wetting envelope, is typically used to predict the suitability of a surface for bonding to an adhesive.³⁹ Knowing the polar and dispersive components of the surface tension of a liquid (e.g. water), one can determine whether that liquid would wet the surface of interest. Points located outside the envelope would suggest that the liquid would not wet the surface well and hence that surface would not be suitable for adhesive bonding. However, information regarding the bond strength of a material adhering to the surface of interest is not provided. Although not quantitative, these plots can still provide useful information in predicting the wetting behavior of liquids, such as water, which can be related to the work of adhesion of the surface with liquid water or ice.

Wetting envelopes for the investigated compositions were generated from data in Table 3 and presented in Figures 8 -10. The receding contact angle data was used since it was suggested by Mueller et. al.³⁸ to be more closely associated with ice adhesion strength relative to advancing or sessile contact angle values. In general, wetting envelopes for the surfaces anticipated to exhibit lower ice adhesion strength, as indicated by the graph in Figure 7, were smaller than the control surface. The wetting envelopes for the C4H and C4H/C11H (50/50) systems (Figure 9) differed from other compositions as well as the control and may be related to the anomalous wetting behavior with water discussed above.

The adhesive of interest in this work, water, has polar and dispersive surface tension values of 51.0 and 21.8 mJ/m², respectively, at 20°C. Based on the wetting envelopes for each of the compositions (Figures 8 – 10), water would not be expected to “wet” the surface. At 0°C the surface energy components (i.e. polar and dispersive) of water are reported to be comparable (52.3 and 23.3 mJ/m², respectively) to the 20°C values.^{40,41} Similar to water at 20°C, water at 0°C would not be expected to fully “wet” these surfaces.

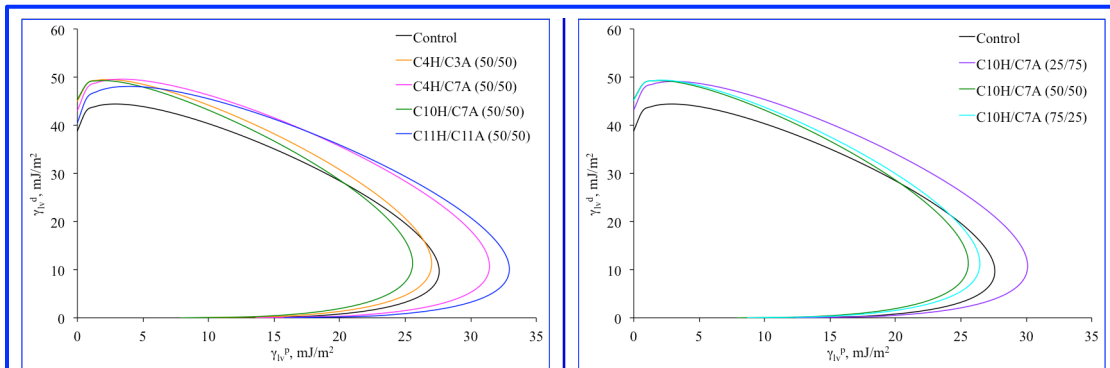


Figure 8 – Wetting envelopes of mixed (C#H/C#A) compositions based on receding surface energy components.

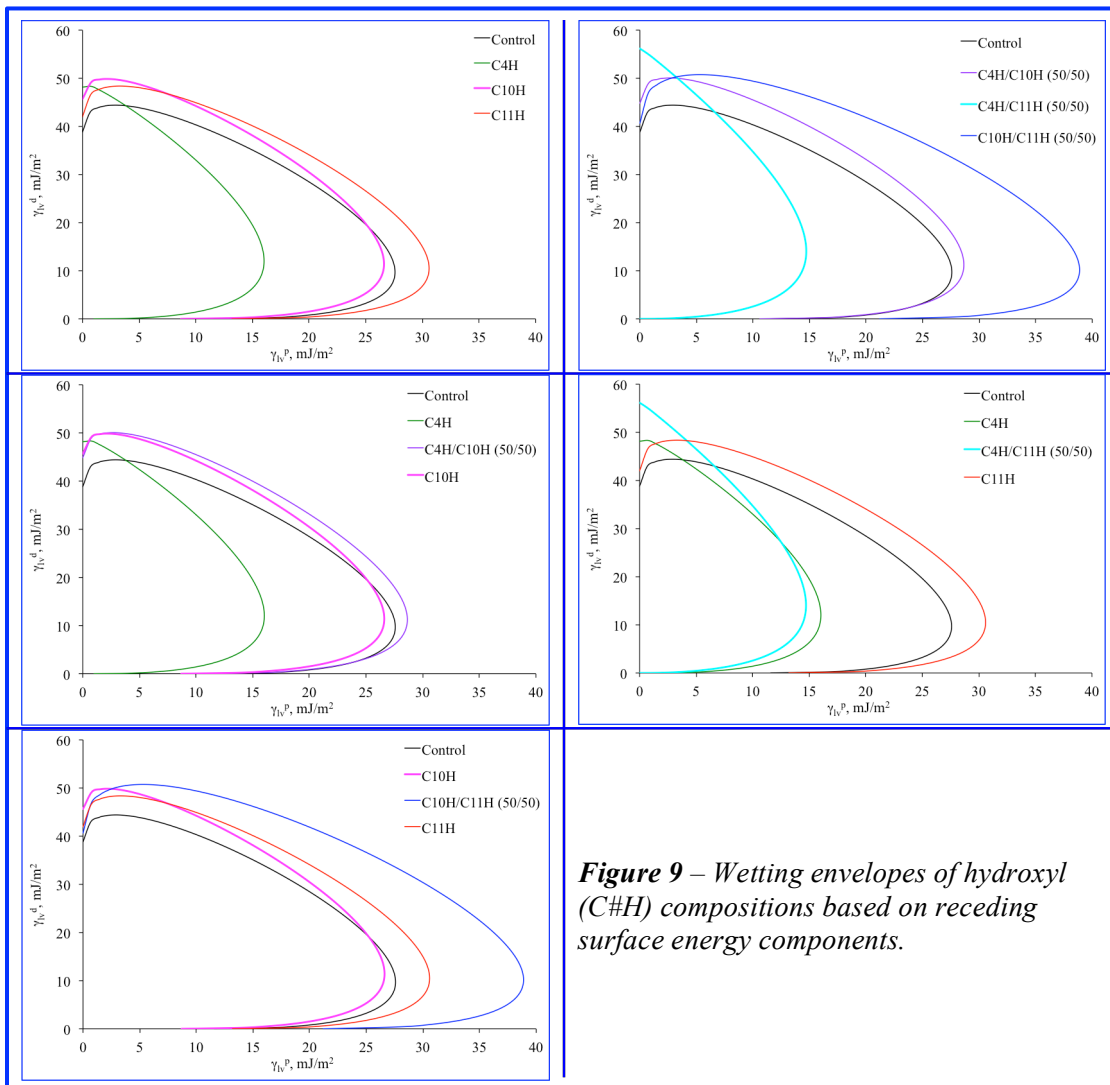


Figure 9 – Wetting envelopes of hydroxyl (C#H) compositions based on receding surface energy components.

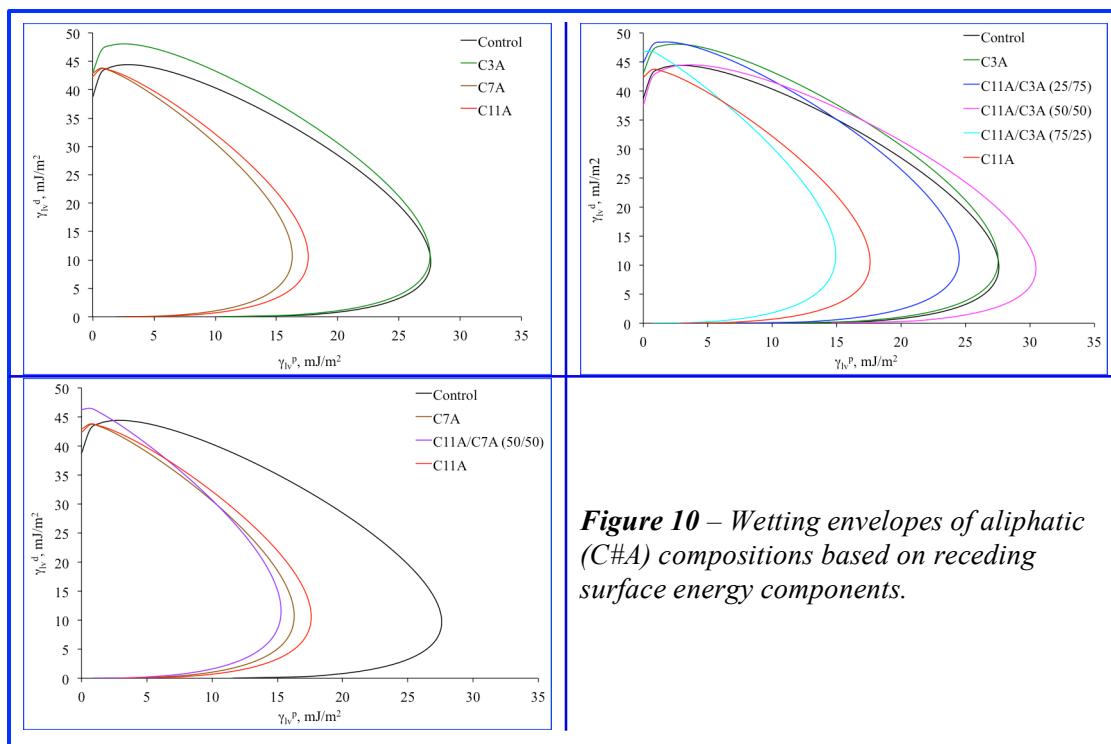
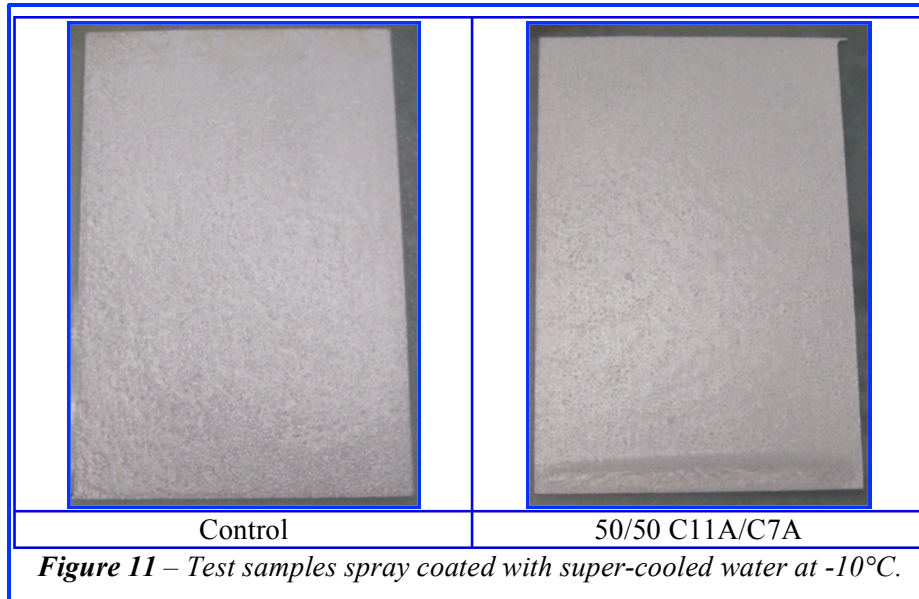


Figure 10 – Wetting envelopes of aliphatic (C#A) compositions based on receding surface energy components.

The polar and dispersive values for ice at 0°C, as calculated from a water-ice system, are 11.4 and 94.6 mJ/m², respectively, implying a more nonpolar surface.⁴¹ Similar to water at 0 and 20°C, ice at 0°C would not be expected to fully wet these surfaces (Figures 8 – 10). Even though water or ice would not be expected to wet these surfaces, nothing can be said about the adhesive strength of ice upon them, although it is likely that in order to bind to the surface, a minimal amount of surface water molecules would need to melt in order to interact with the surface in a more favorable geometry (i.e. QLL). Considering this, the wetting dynamics, as described, may provide insight into these interactions.

Qualitative Icing Experiments

It is known that the relationship between ice accretion, adhesion, and shedding is a complex process that is poorly understood. Temperature, substrate properties, and formation mechanism are some of the variables known to affect ice adhesion. Many experimental methods are available to measure ice adhesion (i.e. icing tunnel located at NASA Glenn Research Center), however the cost and complexity is proportional to the TRL⁴² of the material. Due to the low TRL of the materials investigated herein (approximately 2-3), qualitative static ice formation studies were investigated by two methods. The first method involved conditioning samples, inclined at approximately 60°, in a sub-zero freezer for about 24 h. Conditioning temperatures ranged from -10 to -20°C. Once conditioned, samples were spray-coated with supercooled distilled water to simulate impact ice or freezing rain. After spray coating, the samples were allowed to statically stand undisturbed at sub-zero temperature for several hours and then visually assessed. Although not an accurate analog for aircraft icing or freezing rain events, it allowed for qualitative observations to be made. For example, visual assessment of mixed aliphatic/hydroxyl compositions tested at -10°C found clear (i.e. glaze) ice formation comparable to that of the uncoated Al control (Figure 11). Even though both samples exhibited a coating of ice, the coated sample (50/50 C11A/C7A) suggested that the supercooled water ran down the surface forming a ridge on the bottom of the panel prior to freezing. Visual observation of the other compositions suggested that the performance was comparable to the control. Results of the coated panels tested at -15°C and -20°C were comparable to the control where the ice was visually clear and opaque, respectively.



The second method evaluated the temperature when water microdroplets freeze upon the surface using an in-house fabricated ice formation stage based on a design described in Li et. al.⁴³ The stage and process schematic are shown in Figure 12. Initially, the position of the digital microscope was too far away from the sample surface to enable magnification sufficient to observe microdroplet formation. This issue was remediated by modification of the digital microscope structure reducing the distance from the objective to the surface. With the new microscope orientation, microdroplets were readily visible on the surface and experimentation was conducted to determine the temperature at which they froze. Once a few preliminary investigations were completed however, the cooling line was determined to be clogged. Since there were extensive elements in place to remove excess water from the low-pressure nitrogen lines, it was determined that a gaseous contaminant, likely carbon dioxide, was solidifying in the copper tubing

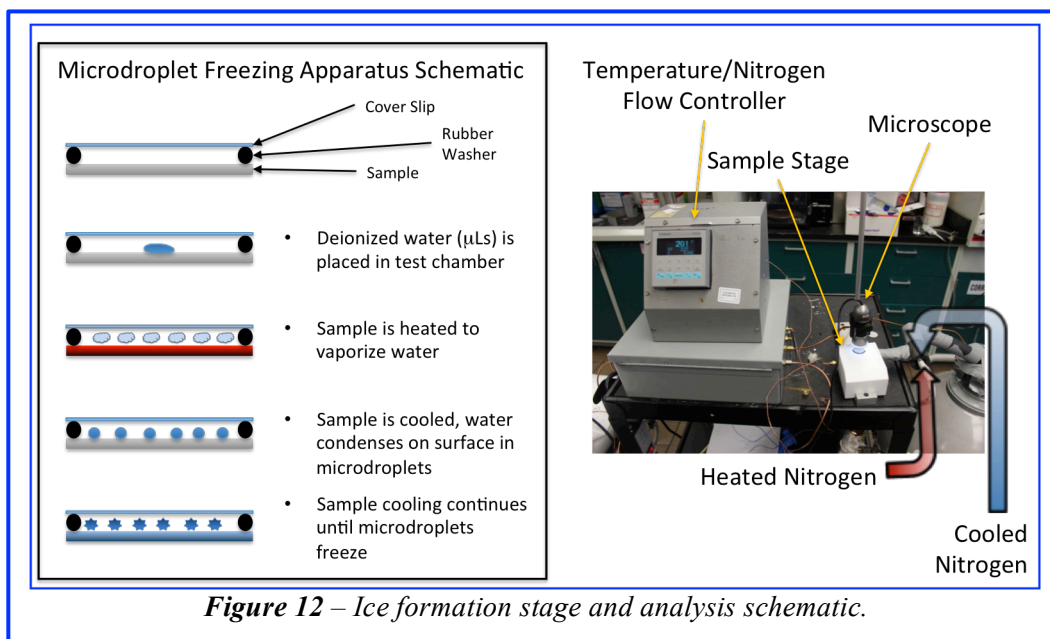
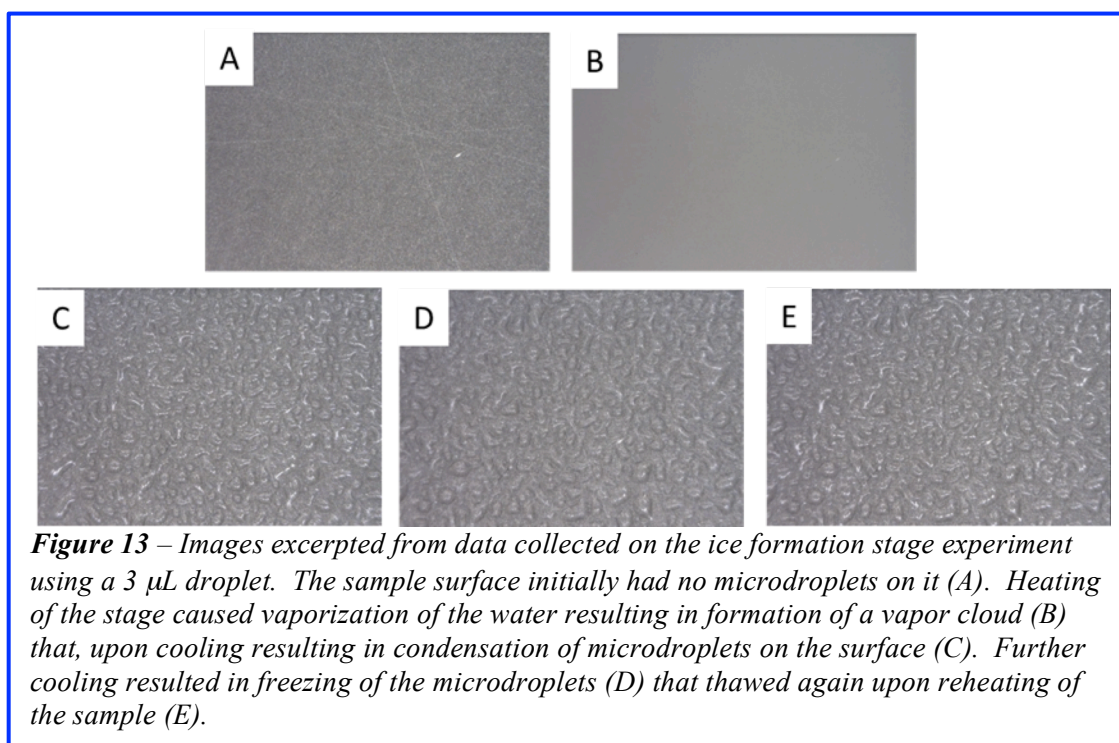


Figure 12 – Ice formation stage and analysis schematic.

coiled in the liquid nitrogen. After changing the diameter of the copper tubing submerged in the liquid nitrogen and only partially filling the Dewar containing the liquid nitrogen, the cooling line was observed to function properly during testing.

Initial experiments were conducted to determine the appropriate volume to use in the microdroplet freezing experiments. In these experiments, the droplet was deposited on the surface using a micropipette or syringe and upon heating, was observed to vaporize resulting in condensation observed on the cover slip (Figure 13). Upon cooling, microdroplet formation was observed on the surface. Freezing was observed upon further cooling by an increase in the opacity of the microdroplets and an increase in the angularity of the microdroplet profiles. Although microdroplets were observed using a 5 μL droplet, these were observed to rapidly coalesce rendering the deposits unusable. Similarly, a 3 μL droplet produced microdroplets but it was determined that these microdroplets were still too large and potentially shared interfacial regions with other microdroplets (Figure 13). Satisfactory results were observed using volumes ranging from 0.5-2 μL with the most repeatable results obtained using 1.5 μL droplets.



While determining the proper droplet volume to use, it was observed that the temperature determined by the thermocouples in the air chamber and in contact with the sample varied significantly: 5.5-8.3 $^{\circ}\text{C}$ in a few seconds. This variation would make it exceptionally difficult to ascertain differences in freezing temperatures on surfaces unless they were markedly different. The thermocouple in the air chamber should vary considerably due to rapid changes in the relative amounts of heated and cooled nitrogen being introduced. The thermocouple in contact with the sample, however, should not and this observation suggested that this thermocouple was reporting the temperature variation of the nitrogen instead of the temperature change of the sample. Several methods to mitigate this complication have been investigated, including taping the thermocouple to the sample surface. Although taping has shown some improvement in signal variation, remediation of this issue is ongoing. Once completed however, the microdroplet freezing stage should enable differentiation between freezing temperatures on the test surfaces of 0.5-1.1 $^{\circ}\text{C}$.

MD Simulations

To gain a molecular level understanding and provide guidance to the synthetic effort, MD simulations were performed to study the impact of chain length, surface modifier composition, and HB groups on the disruption of ice formation and QLL formation and growth. Simulations were run using the open source code LAMMPS due to its versatility and its scalability.²⁵ The Nosé-Hoover thermostat²⁶ was implemented in all simulations to maintain temperature in a constant number of molecules, volume, and temperature (NVT) ensemble at 230 K. Rozmanov and Kusalik found this temperature was ideal for the growth and maintenance of an ice crystal.⁴⁴ The TIP4PQ/2005¹³ model for water was used since it produces the most accurate simulated ice structures compared to experiments.^{29,30} This model was a refinement of the original TIP4P model,⁴⁵ where water is depicted as a neutral oxygen atom connected to two mass-less, but positively charged, hydrogens and a mass-less negatively charged entity placed along the angle bisector to best represent the dipole moment of water. For every surface studied, a total of 3360 water molecules were placed on a lattice matching an ice crystal in the wurtzite hexagonal phase, ice-Ih.

Heuristics for modeling ice in the presence of a HB surface began with construction of a silica substrate and placement of the ice crystal. Silica was chosen instead of Al, as used experimentally, due to lack of force field parameters required for modeling metals with organics. Utilizing the Dreiding force field²⁷, the silica substrate was constructed from a wurtzite crystal structure. Initially, the ice was directly inserted between two solid surfaces (Figure 14). The HB network in the presence of these two layers was

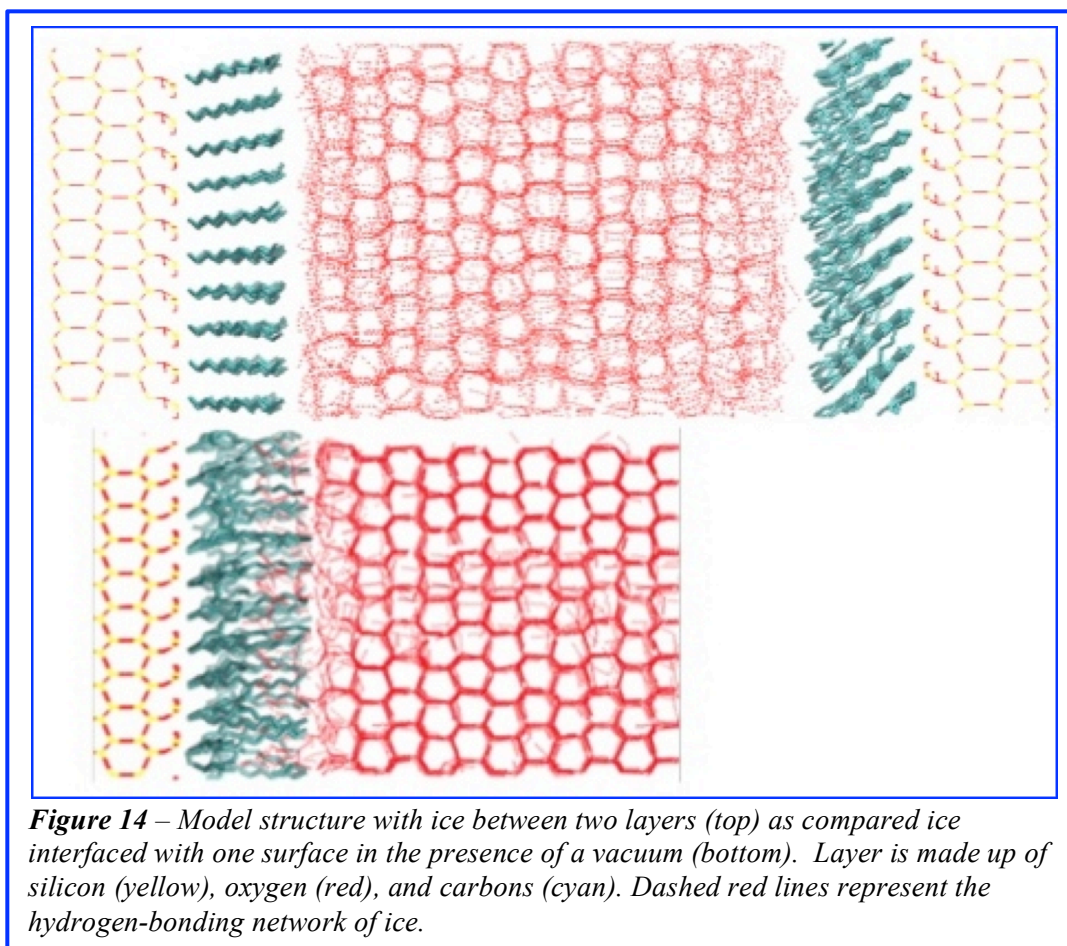


Figure 14 – Model structure with ice between two layers (top) as compared ice interfaced with one surface in the presence of a vacuum (bottom). Layer is made up of silicon (yellow), oxygen (red), and carbons (cyan). Dashed red lines represent the hydrogen-bonding network of ice.

immediately and artificially disrupted, as indicated by the faint lines representing HB between waters, as opposed to the bold lines of the HB network for the single surface simulation. These preliminary runs demonstrated the difficulty of guessing the proper separation distance *a priori*. In prior work,⁴⁶ ice is grown, rather than inserted, between surfaces; the surfaces investigated here presumably prevent or inhibit ice growth, so an alternative approach had to be chosen.

To overcome the issue with separation distance, the ice crystal was first placed at a distance far from a singular surface (approximately 8 Å). Periodic boundary conditions were applied parallel, but not normal, to the surface so that the backside of the ice crystal was exposed to a vacuum rather than another surface. As such, a pressure controller was not necessary, allowing a constant volume ensemble to be utilized instead. At this initial placement, the interactions between the surface and the crystal began to dictate the dynamics and spacing, allowing for a more natural separation distance. In order to minimize any stress due to impact and similar artifacts, the temperature was maintained well below the freezing point (100 K) and a viscous term was added to the velocity of all the water molecules. The viscous term acted like an artificial friction factor to prevent the waters from unnaturally accelerating when it came into contact with the surface. As soon as the crystal stabilized, the viscous term was removed. The temperature was slowly increased to 230 K and the integration time step increased to a value of 1.0 fs. This approach was very costly in terms of simulation time, but was found to be necessary if a proper interface was to be established (as seen in the other half of Figure 14). Once stability of the interface was achieved, the system was run for an additional 2.0 ns to observe the effects of the surface upon the ice crystal.

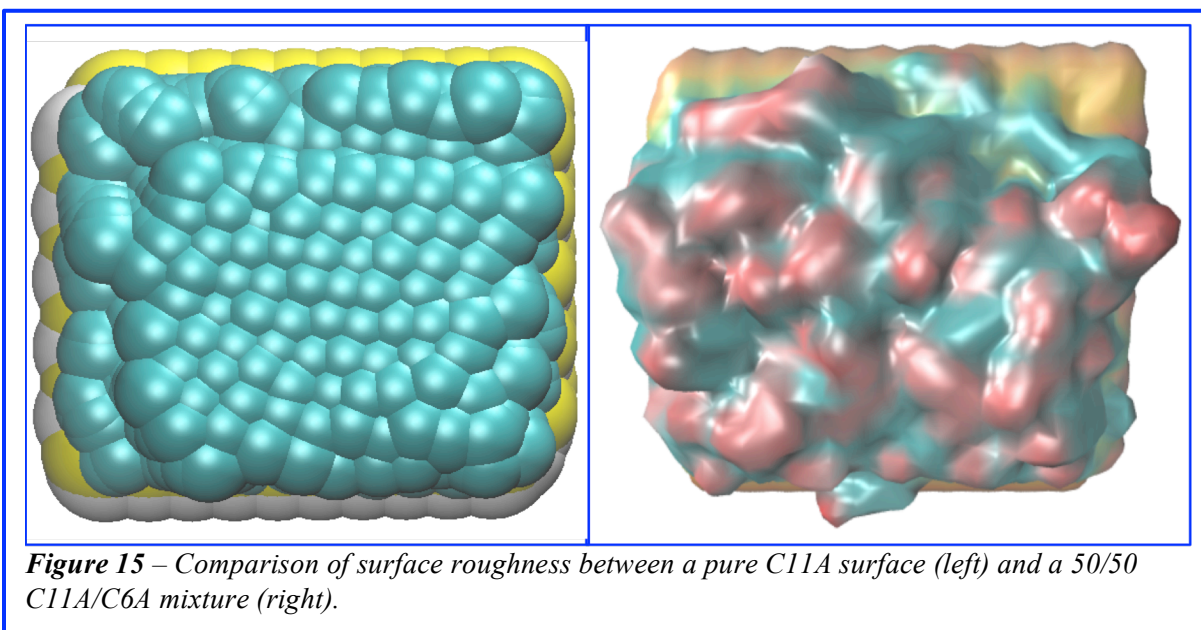
Once the methodology for insertion of the ice crystal was established, codes were developed to bond modifiers to the silica substrate. The bonding configuration of the silica substrate to the modifier system used a combination of the Dreiding force field²⁷ (for carbon backbone atoms and the silica substrate) and the Charmm General Force Field (CGenFF)²⁸ for the HB functional groups. While mixing force fields may present problems, earlier unpublished work with self-healing polymers found it to be necessary to model the HB efficiently and accurately. The Dreiding force field is a generic united atom force field (carbons with their hydrogens modeled as one site) capable of modeling polymer systems.²⁷ CGenFF has proven to be effective for modeling HB functional groups.²⁸ Additionally, CGenFF is also optimized to best interact with current water models. Using these codes, 100 C11A modifiers were attached to the substrate.

These initial codes could not be applied to modifier mixtures due to difficulties in accounting for differences in chain length. Rather, the C11A chains were modified within the code to obtain the desired mixture ratio, chain length, and functionality of the different surface compositions. Specifically, atom entries were removed from the configuration file to shorten chain lengths and the entries for terminal carbons were replaced with an oxygen and a hydrogen for alcohol functionalization. After addressing these issues the following systems were constructed: bare silica, C11A, C11H, and mixtures of a) C11A and C6A, b) C11H and C6H, and c) C11H and C6A in ratios of 50/50, 25/75, and 75/25.

Simulated surface modifiers were characterized by measuring surface roughness and terminal site mobility. In order to evaluate surface roughness for the compositions studied herein, methods from geology for measuring terrain roughness were adapted. For terrain, the elevation can easily be measured, but within a molecular model, identifying which atoms make up the surface can be difficult. First, the atom with the largest z-value (distance from surface) was identified and stored. Centered on this atom, a cylindrical shell of infinite height and a radius of 2.0 Å was placed over the simulation cell. Any atoms within the cylinder were assumed to be under the atom of interest and deleted from the list of “surface atoms”. This process was repeated until all of the atoms were either deleted or stored as a surface atom. These surface atoms represented where elevation points would be collected for terrain. Three different methods were then employed to characterize surface roughness.

The first method involved standard deviation of height from the substrate. A large difference in height afforded a large standard deviation suggesting a rough surface. However for a perfectly patterned surface consisting of large areas of long chains and large areas of short chains the standard deviation would still be high, but the surface may not appear rough. The second method was based on the Terrain Ruggedness

Index (TRI)⁴⁷ which accounts for localized roughness. At each nodal point (i.e. a surface atom) the method takes the average height of each nearest neighbor (i.e. atoms within 4.0 Å). The difference between the nodal point and the average height of the neighbors was then recorded and averaged over all of the surface sites. The third method characterized surface roughness as the standard deviation of surface slope. Using the surface atoms as vertices, a triangular mesh was placed over the surface, similar to what is done in finite element analysis. The roughness was subsequently characterized as the standard deviation of the slopes of all the triangular planes. The magnitude obtained by these three methods was different for each surface. For example, the first method had a value of 1.266 while the third method was 0.209 for the pure C11A surface. As such, the reported roughness values were normalized to values for C11A to give each method equal weighting. In addition, qualitative roughness could be compared through topological diagrams like those shown in Figure 15.



Initial work was performed with a pure C11A surface and mixtures of C11A/C6A, with the results for surface roughness, chain mobility, and QLL presented in Figure 16. When measuring the surface roughness in the presence of a vacuum compared to an ice crystal, a small percentage of long chains in the C11A/C6A (75/25) mixed system resulted in a larger roughness factor. The isolated short C6A chains made for isolated regions of pockets (i.e. valleys). The next roughest surface was afforded by the 25/75 mixed system where isolated regions of high roughness (i.e. peaks) afforded by the long chains. The 50/50 composition exhibited the lowest roughness of the mixed systems due to an even population of valleys and peaks on the surface.

In the presence of ice, the surface roughness changed due to interaction with the water molecules. Keeping pure C11A as the normalization standard (i.e. 1.00), the normalized roughness for the C11A/C6A surfaces of 25/75, 50/50, and 75/25 were 1.48, 0.98, and 0.92, respectively (Figure 16). For the 75/25 case, the presence of ice appeared to alter the surface roughness in unpredictable ways affording the least rough surface. A similar effect was observed with the 50/50 system, which was comparable to the pure C11A surface. The 25/75 composition appeared to be the least effected by the presence of ice compared to the vacuum condition and was approximately 50% rougher compared to the pure C11A surface.

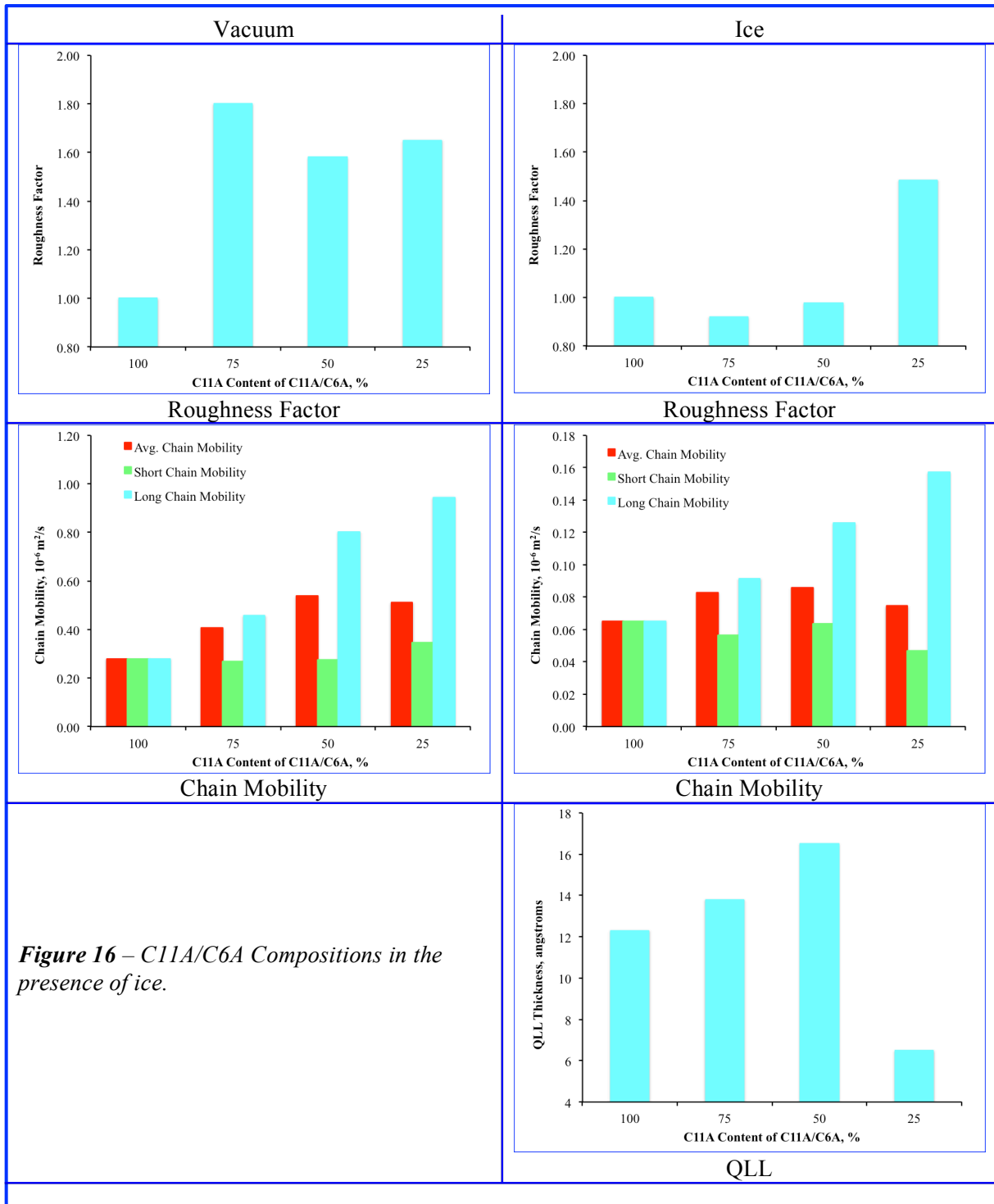


Figure 16 – C11A/C6A Compositions in the presence of ice.

Chain mobility was characterized by MSD, which is defined by the Einstein-Stokes equation (1):

$$MSD = \frac{\langle \Delta r \rangle^2}{6\Delta t}, \quad (1)$$

The brackets represent an ensemble average and Δr represents the change in position over a certain timeframe, Δt . Performing the simulations under vacuum conditions as described above, the average chain mobilities for the pure C11A system and the mixed C11A/C6A (50/50) system were $0.2789 \times 10^{-6} \text{ m}^2/\text{s}$ and $0.5380 \times 10^{-6} \text{ m}^2/\text{s}$, respectively. However, in the presence of ice the average chain mobility decreased approximately 80% to 0.0652×10^{-6} and $0.0860 \times 10^{-6} \text{ m}^2/\text{s}$ for the pure C11A and mixed C11A/C6A (50/50) systems, respectively. This suggested that water molecules present in the QLL dampened chain mobility because much of the momentum was transferred from the flailing chain to the water. A comparison of the C11A and mixed C11A/C6A surfaces in the presence of ice and vacuum are shown in Figure 16. The transfer of momentum from the chains to the water was largest for the mixed C11A/C6A 50/50 and 75/25 compositions compared to the pure C11A system partly due to water “trapped” or absorbed into the layer. Due to this large difference from the vacuum values, only chain mobility in the presence of ice will be reported.

Considering just the long chain (C11A) mobility for the mixtures, Figure 16 shows how the C11A mobility (i.e long chain) increased for decreasing C11A content in a linear fashion ($r^2 = 0.9974$). For the C11A/C6A (25/75) mixture this was an approximate 240% increase compared to the 100% C11A surface. The long chains in the C11A/C6A (25/75) mixture have a higher mobility overall because the voids are much larger. In a sense, the chains are completely isolated and have the mobility of a typical long chain alkane in solution. The effect of this can be seen with this system (25/75) displaying the largest roughness factor. The effect upon short chain mobility for increasing C6A content was not as pronounced as the C11A mobility and was not linear. The highest short chain (C6A) mobility was displayed by the 50/50 composition followed by the 75/25 and 25/75 systems.

C11A and C6A chain mobilities would not be expected to act independent of one another in these mixed systems. Therefore the chain mobilities for the long and short chains were average based on the content of each in the respective composition and reported as the average chain mobility. In doing so, the C11A/C6A (50/50) system exhibited the highest average mobility. In the C11A/C6A (50/50) system, the C11A chains are approximately 92% more mobile than the pure C11A system. The mobility of the short C6A chains for the C11A/C6A (50/50) system are of comparable magnitude to the pure C11A system, because they have a similar confinement due to van der Waals (VDW) forces and steric hindrances. Consequently, the *average* mobility for the C11A/C6A (50/50) system is 32% greater than the pure C11A system. The average chain mobility of the C11A/C6A (75/25) and (25/75) systems were 27 and 14%, respectively, larger than the pure C11A system. Overall the increase in average chain mobility was due to the inherent pockets that were generated by the lower content of C11A present in these compositions.

The effects of average chain mobility and surface roughness upon the QLL were subsequently determined. To characterize the QLL, three characterization methods were used. First, density, as a function of distance from the surface, suggested which phase the water was in. Second, MSD, as described earlier, indicated the mobility of water at different distances. Higher mobility was associated with the QLL, while relatively motionless atoms were associated with the crystalline ice phase. Thirdly, a structural order parameter, F_4 , was used.^{48,49} The F_4 structural-order parameter characterizes the type of tetrahedral HB network adopted by the water:

$$F_4 = \langle \cos(3\phi) \rangle. \quad (2)$$

Specifically, a value of -0.4 indicated the water was in an ice state while a value of -0.04 indicated a liquid state.²⁶ In equation (2), ϕ is the dihedral angle measured between two neighboring oxygen atoms and the outermost hydrogen atoms and the average of $\cos(3\phi)$ is the order parameter.

Comparing the density (Figure 17a) between the QLL phase and the ice phase, the density magnitudes had an obvious shift when comparing water near the surface to water far from the surface (crystalline ice). When comparing bulk water to ice, the density should go down. In this case, the density increased at the shift. There have been previous studies, including one by Paesani and Voth,⁵⁰ in which the QLL appeared to also have a lower density compared to the bulk ice, but its small thickness made it difficult to make a solid conclusion.

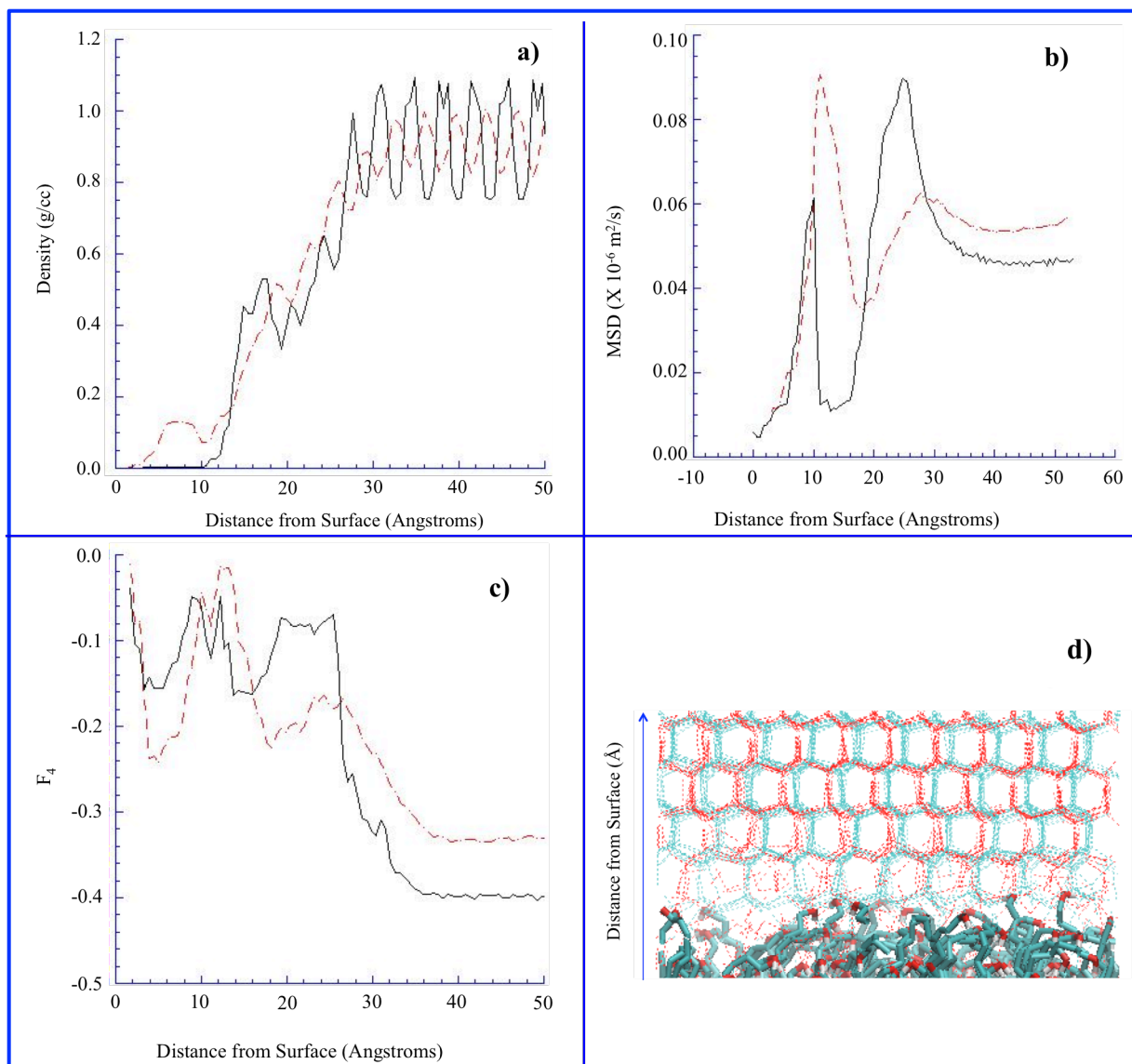


Figure 17 – Quantitative comparison between pure C11A modifiers (solid black) and a 50% mixture of C11A and C6A modifiers (dashed red lines) for ice density (a), MSD (b), and F₄ (c). (d) Qualitative comparison of HB network between pure modifiers (blue dashed lines) and mixed modifiers (red dashed lines).

A possible thermodynamic explanation for the reduced density in the QLL is that the entropic contribution, via a volume expansion, to the Gibbs free energy must increase within the QLL because the enthalpic contribution decreased. The enthalpic contribution is smaller because the water molecules cannot exhibit a good HB network due to the presence of a surface. The water molecules on the edge formed HB networks with only a few water molecules, but not enough to maintain the crystalline network of ice. As such, entropic effects, liquefying, became dominant. For liquid water and QLL water, the enthalpy should be similar. Due to the drop in temperature, as compared to room temperature water, the entropy had to be much larger in the QLL state than for the liquid water to maintain a similar Gibbs free energy and enthalpy levels. To increase the entropy, the density must be much lower than typical liquid water to allow for more microstates.

Independent of the density differences between the QLL and bulk ice phase, the trend for both systems was the same. For the two systems (C11A and 50/50 C11A/C6A) shown in Figure 16, this shift occurred at a greater distance for the mixed system than the pure system. As stated earlier, this indicated that the QLL was much larger for the mixed 50/50 system.

More insight was provided as to why the QLL was much larger by comparing the MSD (Figure 17b) and F_4 (Figure 17c) of water. Near the surface in a QLL state, water will be more mobile because the HB network does not keep the water molecules bound and confined as found in the ice state. As such, a similar shift in MSD was observed as was seen for density. Due to the increased average mobility of the chains for the C11A/C6A (50/50) system (Figure 16), the water molecules experienced difficulty in maintaining a proper HB network in the ice phase. That extra mobility caused the water molecules to break free of the network and switch to a QLL state. The water molecules remaining in the ice state were able to remain there because they are far enough away from the surface to prevent interaction with the flailing chains. Due to the lower average chain mobility of the pure C11A system, the impact on the water molecule was not as great compared to the C11A/C6A (50/50) composition.

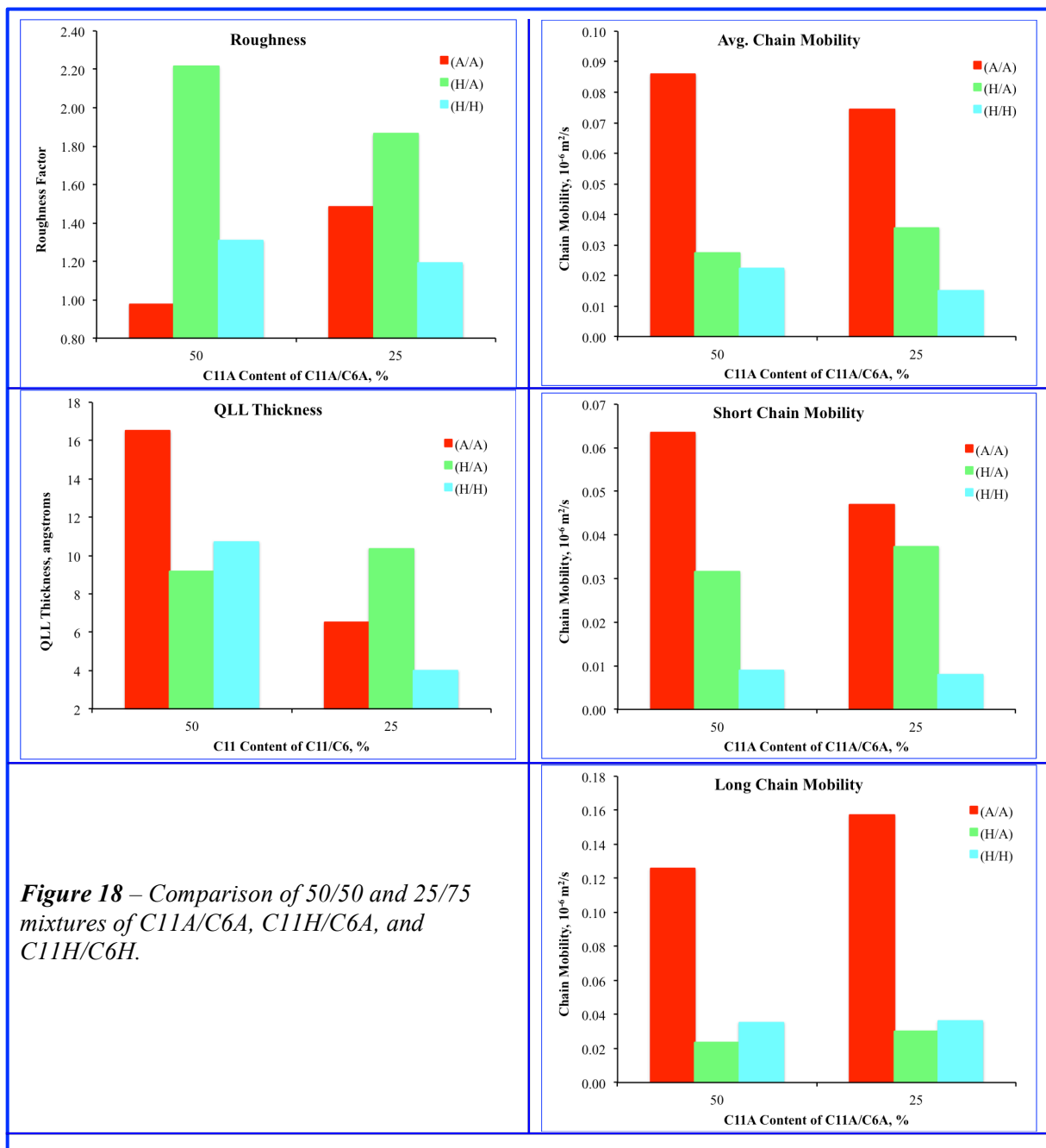
This disruption was also seen when comparing the F_4 factors of the two systems and a visual representation of the HB network (Figure 17d). The F_4 factor numerically characterizes the HB network of the water. At high values, the network was characterized as loosely established. Specifically, ice had an average value of -0.4 while liquid bulk water had an average value of -0.04. The increased disruption of the water by the flailing chains of the C11A/C6A (50/50) system prevented water from forming a proper HB network, even at distances where it typically could be in an ice state, as was seen in the pure C11A system. Without well-established HB between water molecules, the ice crystal can slide against the surface with less resistance as it is only bound by VDW interactions and a few HB. In addition, more mobile waters, as measured by MSD, allowed the QLL to better lubricate the interface between ice and the surface. Finally, the larger volume of water with a lower density minimized how well the water could act as an adhesive to keep the ice crystal bound to the surface. As such, the enhanced QLL, due to these three factors, would presumably diminish the adhesion strength of ice to prevent problematic ice growth at the macroscopic level.

From these measurements, the QLL thickness was identified by the transition point between the QLL state and the ice state. The high average chain mobility of the C11A/C6A (75/25) and (50/50) systems led to QLL values that were 12% and 34% larger, respectively, than the pure C11A system (Figure 16). The QLL for the pure C6A system was not determined but was expected to be comparable to C11A. However, the C11A/C6A (25/75) composition exhibited a QLL thickness that was approximately 50% of the QLL thickness afforded by the pure C11A system. This was surprising given that this composition possessed the largest surface roughness. Of the three C11A/C6A systems, the 25/75 composition exhibited the lowest average chain mobility. This result for the A/A system suggests that chain mobility and not surface roughness would lead to an increase in QLL thickness.

To determine the effect that HB groups (i.e. hydroxyls) had upon the QLL, surface roughness, and chain mobility regarding ice growth, MD simulations were performed on a 50/50 and 25/75 mixtures of a) alkanes (C11A/C6A), b) hydroxyls (C11H/C6H), and c) a mixture of hydroxyls and alkanes (C11H/C6A), with the results shown in Figure 18. As previously stated, surface roughness values were

normalized to the 100% C11A surface. In general, the mixed C11H/C6A compositions afforded a much rougher surface than either the pure H/H or A/A systems. Roughness generally decreased with decreasing C11 content with the exception of the pure A/A system, which may be due to the lack of HB in the pure A/A system.

Comparing the average mobility of the C11/C6 chains, the A/A system displayed the highest mobility due to the lack of HB with water and between neighboring modifiers. The H/H compositions exhibited the lowest average chain mobility. The decreased mobility could be associated with HB between neighboring endgroups, similar to what was observed by Jung *et al.*; they “stick” to the water and to each other.⁵¹ Both



the A/A and H/H systems possessed lower average chain mobility with decreasing C11 content. This decrease was more pronounced for the H/H system (32%) than the A/A system (13%). The H/A system displayed an opposite trend; for decreasing C11H content, the average chain mobility increased approximately 30% due to decreasing HB between neighbors. In general, this supports the observed trend with receding water contact angle data shown in Figure 7, where the A/A systems exhibited the highest contact angles due to a lack of HB. A similar trend was observed regarding short chain (C6) mobility. For decreasing C11 content the long chain mobility increased by 25-30% for the A/A and H/A systems. The reason for the greater C11H long chain mobility at decreasing C11H content for the H/A was the decreasing HB between neighbors (i.e. increased distance between HB groups) and water. The effect upon long chain mobility was not observed with the H/H compositions since there would be no change with HB with water.

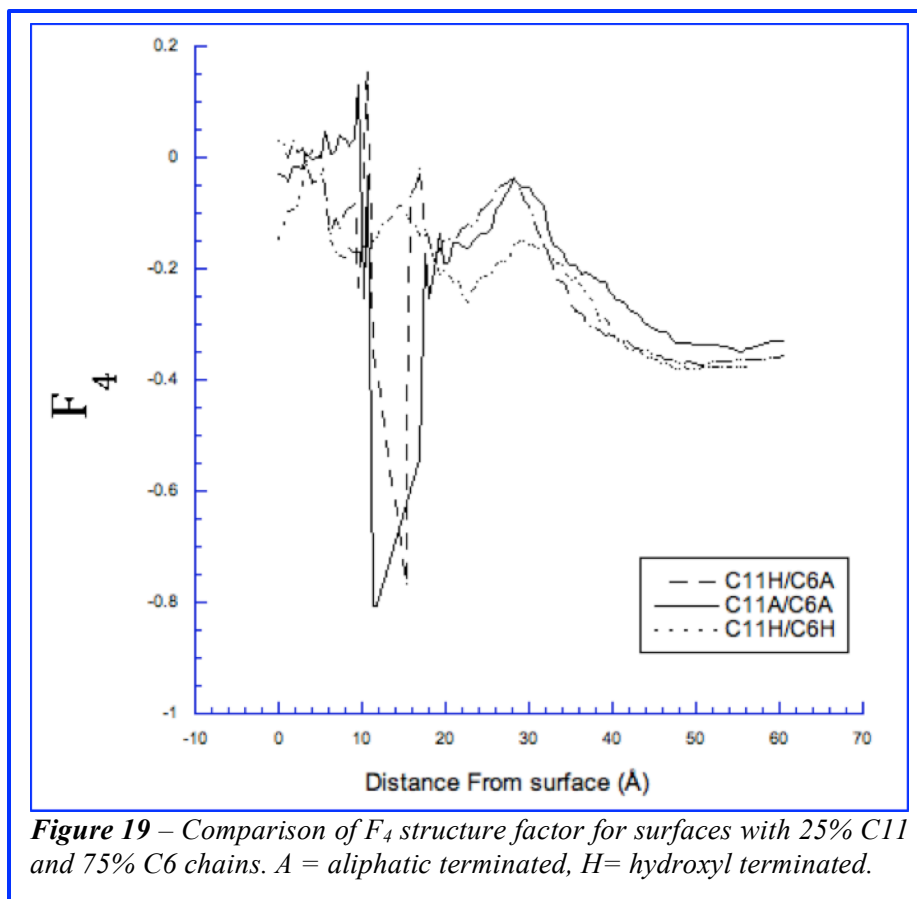
The effect of HB upon the QLL thickness was composition and C11 (i.e. long chain) concentration dependent. For the 50/50 C11/C6 compositions the QLL thickness decreased in the order of A/A > H/H > H/A. This order changed to H/A > A/A > H/H for the 25/75 systems, which may be due to individual C11H chains of the H/A composition being able to interact more freely with water than with neighboring C11H groups.

Similar to the A/A system, the H/A system displayed a greater QLL thickness when there was high average chain mobility and low surface roughness. However this effect occurred with the C11H/C6A (25/75) composition instead of the C11A/C6A (50/50) composition. For the H/H system, a thick QLL was found to be dependent upon high chain mobility and high surface roughness that was associated with the 50/50 composition.

Previous work²³ suggested alcohols would promote ice growth and be a poor choice for an anti-icing functionality. The reason put forth was that HB allowed for ice to bind better to the hydroxyl surface, thus providing a seed for nucleation. The analysis herein suggested that HB was neither detrimental nor beneficial. The pure alkane system (A/A) performed better than either hydroxyl containing systems, but this stems from the higher mobility displayed by the pure alkane system rather than the difference in HB. From simulations, the hydroxyl groups appeared to HB between themselves and water. As such, they were less mobile and had a minimal effect on water.

As mentioned in the experimental section, simulations were run for 2.0 ns after the equilibration period. To determine if sufficient time had been allowed for QLL growth, both the C11A/C6A (50/50) and the C11H/C6H (50/50) were run for an additional 13.0 ns, for a total of 15.0 ns. While little to no change occurred for the alkane mixture after 2.0 ns, the QLL for the C11H/C6H (50/50) system continued to grow, although very slowly, for an additional 8.0 ns. The thicknesses of the two systems were within 1% at that time. This was attributed to the difference in chain length that allowed for more chain mobility and higher free volume of the longer chains. In this case, the free volume was the direct contributor to the anti-icing effect.

The result for QLL thickness C11A/C6A (25/75) system (Figures 16 and 18) was of interest since it was approximately 50% of the C11 value. Looking at F_4 as a function of distance (Figure 19) the value of bulk ice was close to -0.33 (for C11A/C6A (25/75)) versus the expected -0.40. The other 25/75 mixtures (C11H/C6H and C11H/C6A) had bulk values close to -0.40 and suggested a more uniform disruption across the whole ice block. In other words, the enhanced mobility of a low concentration of long chains as displayed by the long chains (C11A) in the C11A/C6A (25/75) system (Figures 16 and 18) may have a longer-range effect with regards to disrupting the HB network of ice. However, this warrants further study.



Conclusions

The effect of HB groups and surface roughness upon ice formation and growth was investigated by coating Al samples with alkyl (A) and hydroxyl (H) terminated surface modifiers. The surface compositions ranged from pure alkyl (A/A) to pure hydroxyl (H/H) as well as a mixture of the two (A/H). Besides the type of endgroup, the effect of chain spacer length between the substrate and terminal functional group was examined to determine the importance of molecular surface roughness. Comparison of the water receding CA revealed several potential candidate materials for further evaluation in ice adhesion studies to be performed in Phase II. In general, qualitative static icing experiments performed in a freezer found no difference in ice formation compared to the control. An exception was the C11A/C7A (50/50) surface which exhibited some run off. MD simulations found that QLL thickness was greatest for non-HB groups and was dependent upon chain mobility and not surface roughness. How this equates with ice adhesion will be determined under Phase II.

Acknowledgements

The authors wish to thank Ron Penner and Dennis Working for their help in the construction of the ice stage.

References

1. Paotapczuk, M.G. Aircraft Icing Research at NASA Glenn Research Center. *J. Aerosp. Eng.* **2013**, *26*, 260-276 and references therein.
2. Lynch, F. T.; Khodadoust, A. Effects of Ice Accretions on Aircraft Aerodynamics. *Prog. Aero. Sci.* **2001**, *37*, 669-767.
3. DeMott, P.J.; Rogers, D.C. Freezing Nucleation Rates of Dilute Solution Droplets Measured between -30°C and -40°C in Laboratory Simulations of Natural Clouds. *J. Atmos. Sci.* **1990**, *47*, 1056-1064.
4. Politovich, M.K. Aircraft Icing in Encyclopedia of Atmospheric Sciences. Academic Press, Oxford, U.K., 2003.
5. Addy Jr., H.E.; Potapczuk, M.G.; Sheldon, D.W. *Modern Airfoil Ice Accretions*. NASA TM-107423, 1997.
6. United States Environmental Protection Agency. *Environmental Impact and Benefit Assessment for Proposed Effluent Limitation Guidelines and Standards for the Airport Deicing Category*. July 2009.
7. Farhadi, S.; Farzaneh, M.; Kulinich, S.A. Anti-Icing Performance of Superhydrophobic Surfaces. *App. Surf. Sci.* **2011**, *257*, 6264–6269.
8. Wang, Y.; Xue, J.; Wang, Q.; Chen, Q.; Ding, J. Verification of Icephobic/Anti-icing Properties of a Superhydrophobic Surface. *ACS Appl. Mater. Interfaces* **2013**, *5*, 3370–3381.
9. Cao, L.; Jones, A. K.; Sikka, V. K.; Wu, J.; Gao, D. Anti-Icing Superhydrophobic Coatings. *Langmuir* **2009**, *25*, 12444–12448.
10. Kulinich, S. A.; Farzaneh, M. How Wetting Hysteresis Influences Ice Adhesion Strength on Superhydrophobic Surfaces. *Langmuir* **2009**, *25*, 8854–8856.
11. Deville, S.; Viazzi, C.; Guizard, C. An Ice-Structuring Mechanism for Zirconium Acetate. *Langmuir* **2012**, *28*, 14892-14898.
12. Grunwald, I.; Rischka, K.; Kast, S.M.; Scheibel, T.; Bargel, H. Mimicking Biopolymers on a Molecular Scale: Nano(bio)technology Based on Engineered Proteins. *Phil. Trans. R. Soc. A* **2009**, *367*, 1727-1747.
13. Anitei, S. Fish 'Antifreeze' Against Icy Aeroplanes. Aug. 8, 2007; <http://news.softpedia.com/news/Fish-Antifreeze-Against-Icy-Aeroplanes-62189.shtml>.
14. Inada, T.; Lu, S.S. Inhibition of Recrystallization of Ice Grains by Adsorption of Poly(Vinyl Alcohol) onto Ice Surfaces. *Crys. Growth Des.* **2003**, *3*, 747-752.
15. Inada, T.; Lu, S.S. Thermal Hysteresis Caused by Non-Equilibrium Antifreeze Activity of Poly(Vinyl Alcohol). *Chem. Phys. Lett.* **2004**, *394*, 361-365.
16. Inada, T.; Modak, P.R. Growth Control of Ice Crystals by Poly(Vinyl Alcohol) and Antifreeze Protein in Ice Slurries. *Chem. Eng. Sci.* **2006**, *61*, 3149-3158.
17. Wang, H.Y.; Inada, T.; Funakoshi, K.; Lu, S.S. Inhibition of Nucleation and Growth of Ice by Poly(Vinyl Alcohol) in Vitrification Solution. *Cryobio.* **2009**, *59*, 83-89.
18. Inada, T.; Koyama, T.; Goto, F.; Seto, T. Ice Nucleation in Emulsified Aqueous Solutions of Antifreeze Protein Type III and Poly(Vinyl Alcohol). *J. Phys. Chem. B* **2011**, *115*, 7914-7922.
19. Anklam, M.R.; Firoozabadi, A. An Interfacial Energy Mechanism for the Complete Inhibition of Crystal Growth by Inhibitor Adsorption. *J. Chem. Phys.* **2005**, *123*, 144708.
20. Nada, H.; Furukawa, Y. Anisotropy in Structural Phase Transitions at Ice Surfaces: A Molecular Dynamics Study. *Appl. Surf. Sci.* **1997**, *121/122*, 445-447.
21. van der Veen, J. F. Melting and Freezing at Surfaces. *Surf. Sci.* **1999**, *433-435*, 1-11.
22. Petrenko, V.F.; Peng, S. Reduction of Ice Adhesion to Metal using Self-Assembling Monolayers. *Can. J. Phys.* **2003**, *81*, 387-393.
23. Dai, Y.; Evans, J.S. Molecular Dynamics Simulations of Template-Assisted Nucleation: Alcohol Monolayers at the Air-Water Interface and Ice Formation. *J. Phys. Chem. B* **2001**, *105*, 10831-10837.
24. Kamat, V. P.; Hagiwara, H.; Katsumi, T.; Hoshi, T.; Suzuki, T.; Ando, M. Ring Closing Metathesis Directed Synthesis of (R)-(±)-Muscone from (+)-Citronellal. *Tetrahedron* **2000**, *56*, 4397-4403.

25. Plimpton, S. Fast Parallel Algorithms for Short-Range Molecular Dynamics. *J. Comp. Phys.* **1995**, 117, 1-19 (1995).
26. Hoover, W.G. Canonical Dynamics: Equilibrium Phase-Space Distributions. *Phys Rev. A* **1985**, 31, 1695-1697.
27. Mayo, S.L.; Olafson, B.D.; Goddard, W.A. DREIDING: A Generic Force Field for Molecular Simulations. *J. Phys. Chem.* **1990**, 94, 8897-8909.
28. Vanommeslaeghe, K.; Hatcher, E.; Acharya, C.; Kundu, S.; Zhong, S.; Shim, J.; Darian, E.; Guvench, O.; Lopes, P.; Vorobyov, I.; Mackerell, A.D. CHARMM General Force Field: A Force Field for Drug-Like Molecules Compatible with the CHARMM All-Atom Additive Biological Force Fields. *J. Comp. Chem.* **2010**, 31, 671-690.
29. Aragoes, J.L.; Noya, E.G.; Abascal, J.L.F.; Vega, C. Properties of Ices at 0 K: A Test of Water Models. *J. Chem. Phys.* **2007**, 127, 154518 1-10.
30. McBride, C.; Vega, C.; Noya, E.G.; Ramirez, R.; Sese L.M. Quantum Contributions in the Ice Phases: The Path to a New Empirical Model for Water-TIP4PQ/2005. *J. Chem. Phys.* **2009**, 131, 024506, 1-13.
31. Green, T. W.; Wuts, P. G. M. *Protective Groups in Organic Synthesis*. Wiley-Interscience, New York, 1999, 127-141, 708-711.
32. Corey, E.J.; Venkateswarlu, A. Protection of Hydroxyl Groups as tert-Butyldimethylsilyl Derivatives. *J. Am. Chem. Soc.* **1972**, 94, 6190-6191.
33. Belyakova, Z. V.; Pomerantseva, M. G.; Efimova, L. A.; Chernyshev, E. A.; Storozhenko, P. A. Effect of Catalysts on the Reaction of Allyl Esters with Hydrosilanes. *Russian J. Gen. Chem.* **2010**, 80, 728-733.
34. Celebuski, J.E. Process for Synthesis of Silyl Alcohols. U.S. Patent 5,113,005, May 12, 1992.
35. Silverstein, R.M.; Bassler, G.C.; Morrill, T.C. *Spectroscopic Identification of Organic Compounds*. John Wiley and Sons, 1981.
36. Davies, J. S.; Higginbotham, C. L.; Tremeer, E. J.; Brown, C.; Treadgold, R. C. Protection of Hydroxyl Groups by Silylation: Use in Peptide Synthesis and as Lipophilicity Modifiers for Peptides. *J. Chem. Soc. Perkin Trans.* **1992**, 1, 3043-3048.
37. Kaelble, D.H. Dispersion-Polar Surface Tension Properties on Organic Solids. *J. Adhes.* **1970**, 2, 66-81.
38. Meuler, A.J.; Smith, J.D.; Varanasi, K.K.; Mabry, J.M.; McKinley, G.H.; Cohen, R.E. Relationships between Water Wettability and Ice Adhesion. *ACS Appl. Mater. Interfaces* **2010**, 2, 3100-3110.
39. Cirlin, E.H.; Kaelble, D.H. Roughness and Anisotropy Effects on Wettability of Polytetrafluoroethylene and Sodium-treated Polytetrafluoroethylene. *J. Polym. Sci. Pol. Phys.* **1973**, 11, 785-799.
40. Van Oss, C.J.; Giese, R.F.; Wentzek, R.; Norris, J.; Chuvilin, E.M. Surface Tension Parameters of Ice Obtained from Contact Angle Data and from Positive and Negative Particle Adhesion to Advancing Freezing Fronts. *J. Adhes. Sci. Technol.* **1992**, 6, 503-516.
41. Kloubek, J. Calculation of Surface Free Energy Components of Ice According to Its Wettability by Water, Chlorobenzene, and Carbon Disulfide. *J. Colloids Interf. Sci.* **1974**, 46, 185-190.
42. Mankins, J.C. *Technology Readiness Levels: A White Paper*. NASA, Office of Space Access and Technology, Advanced Concepts Office, April 6, 1995.
43. Li, K.; Xu, S.; Shi, W.; He, M.; Lo, H.; Li, S.; Zhou, X.; Wang, J.; Song, Y. Investigating the Effects of Solid Surfaces on Ice Nucleation. *Langmuir* **2012**, 28, 10749-10754.
44. Rozmanov, D.; Kusalik, P.G. Temperature Dependence of Crystal Growth of Hexagonal Ice (Ih). *Phys. Chem. Chem. Phys.* **2011**, 13, 15501-15511.
45. Jorgensen, W.L.; Chandraskhar, J.; Madura, J.D.; Impey, R.W.; Klein, M.L. Comparison of Simple Potential Functions for Simulating Liquid Water. *J. Chem. Phys.* **1983**, 79, 926-935.
46. Bai, D.; Chen, G.; Zhang, X.; Wang, W. Microsecond Molecular Dynamics Simulations of the Kinetic Pathways of Gas Hydrate Formation from Solid Surfaces. *Langmuir* **2011**, 27, 5961-5967.

47. Riley, S.J.; DeGloria, S.D.; Elliot, R. A Terrain Ruggedness Index that Quantifies Topographic Heterogeneity. *Intermountain J. Sci.* **1999**, *5*, 1-4.
48. Rodger, P.M.; Forester, T.R.; Smith, W. Simulations of the Methane Hydrate / Methane Gas Interface near Hydrate Forming Conditions. *Fluid Phase Equil.* **1996**, *116*, 326-332.
49. Báez, L.A.; Clancy, P. Computer Simulation of the Crystal Growth and Dissolution of Natural Gas Hydrates. *Ann. N.Y. Acad. Sci.* **1994**, *715*, 177-186.
50. Paesani, F.; Voth, G.A. Quantum Effects Strongly Influence the Surface Premelting of Ice. *J. Phys. Chem. C* **2008**, *112*, 324-327.
51. Jung, S.; Dorrestijn, M.; Raps, D.; Das, A.; Megaridis, C.M.; Poulikakos, D. Are Superhydrophobic Surfaces Best for Icephobicity?. *Langmuir* **2011**, *27*, 3059-3066.

REPORT DOCUMENTATION PAGE

*Form Approved
OMB No. 0704-0188*

The public reporting burden for this collection of information is estimated to average 1 hour per response, including the time for reviewing instructions, searching existing data sources, gathering and maintaining the data needed, and completing and reviewing the collection of information. Send comments regarding this burden estimate or any other aspect of this collection of information, including suggestions for reducing this burden, to Department of Defense, Washington Headquarters Services, Directorate for Information Operations and Reports (0704-0188), 1215 Jefferson Davis Highway, Suite 1204, Arlington, VA 22202-4302. Respondents should be aware that notwithstanding any other provision of law, no person shall be subject to any penalty for failing to comply with a collection of information if it does not display a currently valid OMB control number.
PLEASE DO NOT RETURN YOUR FORM TO THE ABOVE ADDRESS.

1. REPORT DATE (DD-MM-YYYY) 01-07-2014		2. REPORT TYPE Technical Memorandum		3. DATES COVERED (From - To)	
4. TITLE AND SUBTITLE Hydrogen-Bonding Surfaces for Ice Mitigation				5a. CONTRACT NUMBER	
				5b. GRANT NUMBER	
				5c. PROGRAM ELEMENT NUMBER	
6. AUTHOR(S) Smith, Joseph G., Jr.; Wohl, Christopher J.; Kreeger, Richard E.; Hadley, Kevin; McDougall, Nicholas				5d. PROJECT NUMBER	
				5e. TASK NUMBER	
				5f. WORK UNIT NUMBER 694478.02.93.02.12.38.23	
7. PERFORMING ORGANIZATION NAME(S) AND ADDRESS(ES) NASA Langley Research Center Hampton, VA 23681-2199				8. PERFORMING ORGANIZATION REPORT NUMBER L-20408	
9. SPONSORING/MONITORING AGENCY NAME(S) AND ADDRESS(ES) National Aeronautics and Space Administration Washington, DC 20546-0001				10. SPONSOR/MONITOR'S ACRONYM(S) NASA	
				11. SPONSOR/MONITOR'S REPORT NUMBER(S) NASA/TM-2014-218291	
12. DISTRIBUTION/AVAILABILITY STATEMENT Unclassified - Unlimited Subject Category 23 Availability: NASA CASI (443) 757-5802					
13. SUPPLEMENTARY NOTES					
14. ABSTRACT Ice formation on aircraft, either on the ground or in-flight, is a major safety issue. While ground icing events occur predominantly during the winter months, in-flight icing can happen anytime during the year. The latter is more problematic since it could result in increased drag and loss of lift. Under a Phase I ARMD NARI Seedling Activity, coated aluminum surfaces possessing hydrogen-bonding groups were under investigation for mitigating ice formation. Hydroxyl and methyl terminated dimethylethoxysilanes were prepared via known chemistries and characterized by spectroscopic methods. These materials were subsequently used to coat aluminum surfaces. Surface compositions were based on pure hydroxyl and methyl terminated species as well as mixtures of the two. Coated surfaces were characterized by contact angle goniometry. Receding water contact angle data suggested several potential surfaces that may exhibit reduced ice adhesion. Qualitative icing experiments performed under representative environmental temperatures using supercooled distilled water delivered via spray coating were inconclusive. Molecular modeling studies suggested that chain mobility affected the interface between ice and the surface more than terminal group chemical composition. Chain mobility resulted from the creation of "pockets" of increased free volume for longer chains to occupy.					
15. SUBJECT TERMS Adhesion; Bonding; Coatings; Hydrogen bonds; Metal surface; Mitigation					
16. SECURITY CLASSIFICATION OF:			17. LIMITATION OF ABSTRACT	18. NUMBER OF PAGES	19a. NAME OF RESPONSIBLE PERSON
a. REPORT	b. ABSTRACT	c. THIS PAGE			STI Help Desk (email: help@sti.nasa.gov)
U	U	U	UU	35	19b. TELEPHONE NUMBER (Include area code) (443) 757-5802